

**THE DEVELOPMENT OF AN EROSIVE BURNING MODEL FOR SOLID  
ROCKET MOTORS USING DIRECT NUMERICAL SIMULATION**

A Thesis

Presented to

The Academic Faculty

by

Brian A. McDonald

In Partial Fulfillment

of the Requirements for the Degree

of Doctor of Philosophy in the

School of Aerospace Engineering

Georgia Institute of Technology

April 2004

**THE DEVELOPMENT OF AN EROSIVE BURNING MODEL FOR SOLID  
ROCKET MOTORS USING DIRECT NUMERICAL SIMULATION**

Approved By:

Dr. Suresh Menon, Advisor

Dr. Jeff Jagoda

Dr. Jerry Seitzman

Dr. Tim Lieuwen

Dr. Robert Hackett

April 21, 2004  
Date Approved

## DEDICATION

*"Worthy are you, our Lord and God, to receive glory and honor and power, for you created all things, and by your will they existed and were created."*

*Rev. 4:11 (English Standard Version)*

## ACKNOWLEDGEMENTS

I am greatly indebted to Dr. Menon and Dr. Jagoda for their willingness to allow me to pursue this degree from a remote location.

I appreciate the countless emails Dr. Menon has answered in advising me in my work. His support and advice in the completion of this research has been most valuable.

I would like to thank Dr. Seitzman for the tutorial session he gave me in preparation of the oral exams. Those two hours were as vital and beneficial as any I received in my educational career.

Thanks to Dr. Lieuwen for serving on my committee.

I am very grateful for Dr. Robert Hackett serving on my committee. He has given support at several key junctures in my career, for which I am much appreciative.

I am also indebted to Eggenspieler Gilles for his ability to take excellent class notes and willingness to share them.

Thank you to Scott Michaels of the U.S. Army Aviation and Missile Command's Propulsion Laboratory for the use of the CKEM data.

I am indebted to Dr. Bill and Anne Stone, of Stone Engineering for all of the mentoring, support, and opportunity they have offered to me at Stone Engineering over the last 15 years.

Special thanks to Dr. Tom Tytula for agreeing to review this Thesis.

I would like to thank my parents, Parris and Arlene McDonald, who provided the means and support to begin this educational journey many years ago.

Finally, my deepest thanks go to my marvelous wife and dearest friend Piper, and my three daughters, Kaleigh, Kelsey, and Sarah. Their love, support, and understanding through many frustrations during the pursuit of this degree have been invaluable.

# TABLE OF CONTENTS

ACKNOWLEDGEMENTS.....	iv
LIST OF TABLES.....	ix
LIST OF FIGURES.....	x
LIST OF SYMBOLS.....	xiii
SUMMARY.....	xvi
CHAPTER 1.....	1
<i>INTRODUCTION.....</i>	<i>1</i>
<i>1.0 Background of Erosive Burning.....</i>	<i>1</i>
<i>1.1 Problem Definition.....</i>	<i>5</i>
<i>1.2 Erosive Burning Mechanisms.....</i>	<i>6</i>
<i>1.3 Literature Review.....</i>	<i>7</i>
<i>1.4 Opportunity for DNS.....</i>	<i>8</i>
<i>1.5 Summary of Content.....</i>	<i>10</i>
CHAPTER 2.....	11
<i>PRESENTATION OF OBJECTIVES.....</i>	<i>11</i>
<i>2.0 Overview of Objectives.....</i>	<i>11</i>
<i>2.1 Objective-1 Develop a Calibrated DNS Computer Code.....</i>	<i>11</i>
<i>2.2 Objective-2 Infinite Rate Chemistry Erosive Burning Model.....</i>	<i>12</i>
<i>2.3 Objective-3 Examination of Constant Surface Temperature Assumption.....</i>	<i>12</i>
<i>2.4 Objective-4 Interior Ballistics Analysis.....</i>	<i>13</i>
<i>2.5 Objective-5 Thermal Boundary Layer Growth Impact.....</i>	<i>13</i>

2.6 Objective-6 DNS Model Universalism.....	14
2.7 Objective-7 Finite Rate Chemistry Model.....	14
CHAPTER 3 .....	16
<i>DNS COMPUTER CODE DEVELOPMENT</i> .....	16
3.0 Introduction.....	16
3.1 Overview of DNS Code.....	17
3.2 Governing Equations .....	17
3.3 Gas Phase Boundary Conditions.....	19
3.4 Thermal Transport Model.....	20
3.5 Gas-Solid Interface.....	21
3.6 Numerical Schemes.....	23
3.7 Code Verification.....	24
CHAPTER 4 .....	28
<i>INTERIOR BALLISTICS CODE DESCRIPTION</i> .....	28
4.0 Introduction.....	28
4.1 Overview of the Interior Ballistics Code .....	29
4.2 Governing Equations .....	29
4.3 Solution Methodology.....	30
4.4 Code Verification.....	32
CHAPTER 5 .....	34
<i>EROSIVE BURNING NUMERICAL ANALYSIS</i> .....	34
5.0 Introduction.....	34
5.1 Overview of Analysis.....	35

5.2 Computational Domain.....	36
5.3.0 Infinite Rate Chemistry Model.....	37
5.3.1 Rocket Motor Configuration.....	38
5.3.2 Constant Surface Temperature Analysis.....	40
5.3.3 Ballistics Analysis Using the Infinite Rate DNS Model.....	42
5.4 Varying Surface Temperature Analysis.....	48
5.5 Universalism of the Infinite Rate Chemistry Model.....	50
5.6 Thermal Boundary Layer Profile Dependency.....	52
5.7.0 Finite Rate Chemistry Model Overview.....	59
5.7.1 Model Definition and Boundary Conditions.....	61
5.7.2 Chemical Mechanism.....	63
5.7.3 Model Calibration Procedure.....	64
5.7.4 Finite Rate Model Results.....	65
5.7.5 Reduced Base Burn Rate Analysis.....	74
5.7.6 Interior Ballistics Results for Finite Rate Model.....	80
CHAPTER 6.....	83
CONCLUSIONS AND FUTURE WORK.....	83
APPENDIX.....	87
TIME DEPENDENT DATA.....	87
REFERENCES.....	90
VITA.....	93

## LIST OF TABLES

Table 1 Physical Properties of The CKEM Solid Propellant and Combustion Gases.....	40
Table 2 Heats of Formation of Considered Species.....	62
Table 3 Finite Rate Model Gas Properties.....	63
Table 4 Finite Rate Chemistry Model Input .....	64
Table 5 Finite Rate Model Results.....	66
Table 6 Results of the Low Rate Analysis.....	74

## LIST OF FIGURES

Figure 1 Window Bomb Strand Burner .....	2
Figure 2 Burn Rate Data for AP/HTPB Propellant with Catocene.....	3
Figure 3 CKEM Measured Chamber Pressure.....	4
Figure 4 Entrance Axial Velocity Profile (m/s).....	25
Figure 5 Converged Exit Velocity Profile (m/s).....	26
Figure 6 Axial Velocity Contours (m/s) .....	26
Figure 7 Pressure Contours (Pa).....	27
Figure 8 Convergence History of Exit Pressure .....	27
Figure 9 Ballistics Code Regression Model Schematic.....	31
Figure 10 Comparison of 3DGE to Static Test Data .....	33
Figure 11 Cross-Flow Computational Domain Schematic.....	37
Figure 12 CKEM Rocket Motor Schematic.....	39
Figure 13 Normalized Burn Rate versus Mach Number .....	42
Figure 14 Internal Ballistics Calculations Using DNS Results .....	43
Figure 15 Thermal Boundary Layer Profiles .....	44
Figure 16 Temperature (K) Contours ( $M=0.$ ).....	45
Figure 17 Temperature (K) Contours ( $M=.1$ ).....	46
Figure 18 Temperature (K) Contours ( $M=.5$ ).....	46
Figure 19 Temperature Profile in the Solid .....	47
Figure 20 Expected Surface Temperature versus Normalized Burn Rate .....	48

Figure 21 Comparison of Thermal Boundary Layer.....	49
Figure 22 Ballistics Analysis of CKEM-9 Using DNS Model.....	51
Figure 23 Normalized Surface Values for the 50% Width Case.....	53
Figure 24 Normalized Surface Values for the 2% Width Case.....	54
Figure 25 Thermal Contours at the Leading Edge of the Propellant (K).....	54
Figure 26 Fixed Surface Temperature Burn Rate Profile.....	56
Figure 27 Entrance Temperature Profile from Isentropic Flow Relationships.....	57
Figure 28 Entrance Temperature Profile with Wall Heat Transfer.....	58
Figure 29 Burn Rate Comparison for Isentropic and Modified Entrance Temperature Profiles.....	59
Figure 30 Near Wall Temperature Profile.....	67
Figure 31 Temperature Profiles out to Thermal Boundary Layer Edge.....	67
Figure 32 Comparison of the AP Decomposition and APd-Binder Flame Thicknesses for $M=0.0$ .....	68
Figure 33 APd-Binder Flame Thickness Comparison for Various Free-Stream Mach Numbers.....	69
Figure 34 AP Decomposition Flame Thickness Comparison for Various Free-Stream Mach Numbers.....	70
Figure 35 Near-Wall Vorticity for Various Free-Stream Mach Numbers.....	71
Figure 36 APd-Binder Flame and Vorticity for $M=0.8$ .....	71
Figure 37 Near Wall Tangential Velocity Profiles.....	72
Figure 38 Comparison of Reaction Rate Gradients to Thermal Gradients.....	73

Figure 39 Comparison of Thermal Gradients Through the APd-Binder Flame for a High Rate and Low Rate Propellant .....	75
Figure 40 Comparison of Vorticity Through the APd-Binder Flame for a High Rate and Low Rate Propellant .....	76
Figure 41 Comparison of Thermal Gradients at the Solid-Gas Interface for a High Rate and Low Rate Propellant.....	77
Figure 42 Temperature Contours for $M=0.0$ ( $K$ ) .....	78
Figure 43 APd-Binder Reaction Rate Contours for $M=0.0$ ( $K$ ) .....	78
Figure 44 Temperature Contours for $M=0.3$ ( $K$ ) .....	79
Figure 45 APd-Binder Reaction Rate Contours for $M=0.3$ ( $K$ ) .....	79
Figure 46 Interior Ballistics Results with Finite Rate Model .....	81
Figure 47 Erosive Burning Rate Compared to the Base Rate.....	82
Figure 48 Entrance Velocity Profile in $Y+$ Coordinate System .....	87
Figure 49 Velocity Fluctuations at $y+=15$ , $M=0.1$ , Over Center of Propellant.....	88
Figure 50 Velocity Fluctuations at $y+=30$ , $M=0.1$ , Over Center of Propellant.....	88
Figure 51 Velocity Fluctuations at $y+=15$ , $M=0.1$ , Near Entrance .....	89

## LIST OF SYMBOLS

### *Roman Letters*

$a$	Speed of Sound (Characteristic Wave Equations)
$c$	Burn Rate Coefficient ( $cP^n$ )
$C_p$	Gas Specific Heat at Constant Pressure
$C_s$	Solid Propellant Specific Heat
$d_i$	Characteristic Wave Velocities (i=1-5)
$E$	Total Energy
$E_a$	Activation Energy for Pyrolysis
$G$	Mass Flux
$k_g$	Gas Conductivity
$k_s$	Solid Propellant Conductivity
$l_l$	Integral Scale Dimension
$l_\eta$	Dissipation Scale
$L_i$	Characteristic Wave Amplitudes (i=1-5)
$M$	Mach Number
$M_\infty$	Free Stream Mach Number
<b>M</b>	Mass Flux from Pyrolysis
$MW$	Molecular Weight
$n$	Burn Rate Exponent
$p$	Pressure
$Pr$	Prandtl Number

$r$	Propellant Burn Rate
$r_e$	Erosive Burn Rate
$R$	Gas Constant
$R_1$	Reaction Rate for AP Decomposition Flame
$R_2$	Reaction Rate for APd and Binder Flame
Re	Reynolds Number
$R_u$	Universal Gas Constant
$T$	Temperature
$T_{ad}$	Adiabatic Flame Temperature
$T_o$	Stagnation Temperature
$T_{Surf}$	Propellant Surface Temperature
$T_{Surfo}$	Propellant Surface Temperature – Zero Cross-Flow
$q$	Heat Flux
$Q$	Propellant Heat of Pyrolysis
$u$	Tangential Velocity
$v$	Normal Velocity
$y^+$	Wall Coordinate

*Greek Letters*

$\alpha$	First Lenoir-Robillard Erosive Burning Constant
$\beta$	Second Lenoir-Robillard Erosive Burning Constant
$\gamma$	Ratio of Specific Heats
$\eta$	Mass Fraction of AP

$\lambda$	Second Coefficient of Viscosity
$\mu$	Viscosity
$\rho_p$	Solid Propellant Density
$\rho$	Gas Density
$\sigma$	Coefficient in Outlet Characteristic Wave Equation
$\tau$	Viscous Stress Tensor

### *Abbreviations*

3DGE	3 Dimensional Grain Evaluation Code
AdKEM	Advanced Kinetic Energy Missile
AMCOM	United States Army Aviation and Missile Command
AP	Ammonium Perchlorate
APd	Decomposed Ammonium Perchlorate
CKEM	Compact Kinetic Energy Missile
DCDA	Dicyandiamide
DNS	Direct Numerical Simulation
HTPB	Hydroxyl-Terminated Polybutadiene
LES	Large Eddy Simulation
NASA	National Aeronautics and Space Administration
RHS	Right Hand Side
SRM	Solid Rocket Motor

## SUMMARY

A method for developing an erosive burning model for use in solid propellant design-and-analysis interior ballistics codes is described and evaluated. Using Direct Numerical Simulation, the primary mechanisms controlling erosive burning (turbulent heat transfer, and finite rate reactions) have been studied independently through the development of models using finite rate chemistry, and infinite rate chemistry. Both approaches are calibrated to strand burn rate data by modeling the propellant burning in an environment with no cross-flow, and adjusting thermophysical properties until the predicted regression rate matches test data. Subsequent runs are conducted where the cross-flow is increased from  $M=0.0$  up to  $M=0.8$ . The resulting relationship of burn rate increase versus Mach Number is used in an interior ballistics analysis to compute the chamber pressure of an existing solid rocket motor. The resulting predictions are compared to static test data.

Both the infinite rate model and the finite rate model show good agreement when compared to test data. The propellant considered is an AP/HTPB with an average AP particle size of 37 microns. The finite rate model shows that as the cross-flow increases, near wall vorticity increases due to the lifting of the boundary caused by the side injection of gases from the burning propellant surface. The point of maximum vorticity corresponds to the outer edge of the APd-binder flame. As the cross-flow increases, the APd-binder flame thickness becomes thinner; however, the point of highest reaction rate moves only slightly closer to the propellant surface. As such, the net increase of heat transfer to the propellant surface due to finite rate chemistry affects is small. This leads

to the conclusion that augmentation of thermal transport properties and the resulting heat transfer increase due to turbulence dominates over combustion chemistry in the erosive burning problem. This conclusion is advantageous in the development of future models that can be calibrated to heat transfer conditions without the necessity for finite rate chemistry. These results are considered applicable for propellants with small, evenly distributed AP particles where the assumption of premixed APd-binder gases is reasonable.

# CHAPTER 1

## INTRODUCTION

### *1.0 Background of Erosive Burning*

The development of erosive burning models for interior ballistics purposes dates back to the 1950's. The primary purpose of these models is to better predict or simulate rocket motor chamber pressure and performance in motors with erosive burning. In most design phases of solid rocket motors, subscale burn rate data, either from strand data, or standard 2x4 inch motors is all that is available. Typically, the burn rate behavior of a given propellant in cross-flow is unknown. Subscale propellant burn rate data is typically collected in a closed bomb such as shown in Figure 1 [1].

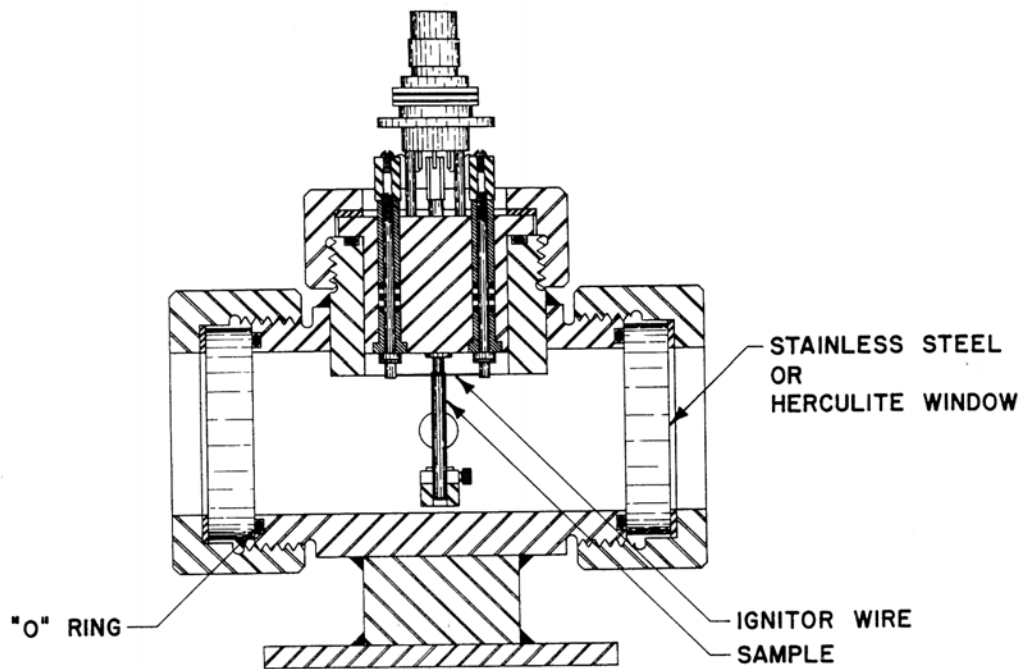


**Figure 1 Window Bomb Strand Burner**

The bombs are pre-pressurized with an inert gas to a selected pressure, and provide a convenient means of characterizing a propellant's burn rate versus pressure. However, the environment is relatively stagnant, and provides no means for inducing a cross-flow at the burning surface. Typical strand burning data is shown in Figure 2<sup>A</sup>.

---

<sup>A</sup> CKEM test data used by permission of the U.S. Army Aviation and Missile Command, Huntsville, AL, 2001, CKEM Program. Program Manager- Mr. George Snyder, Chief Engineer – Mr. Steve Casan, and Propulsion Lead – Mr. Scott Michaels.

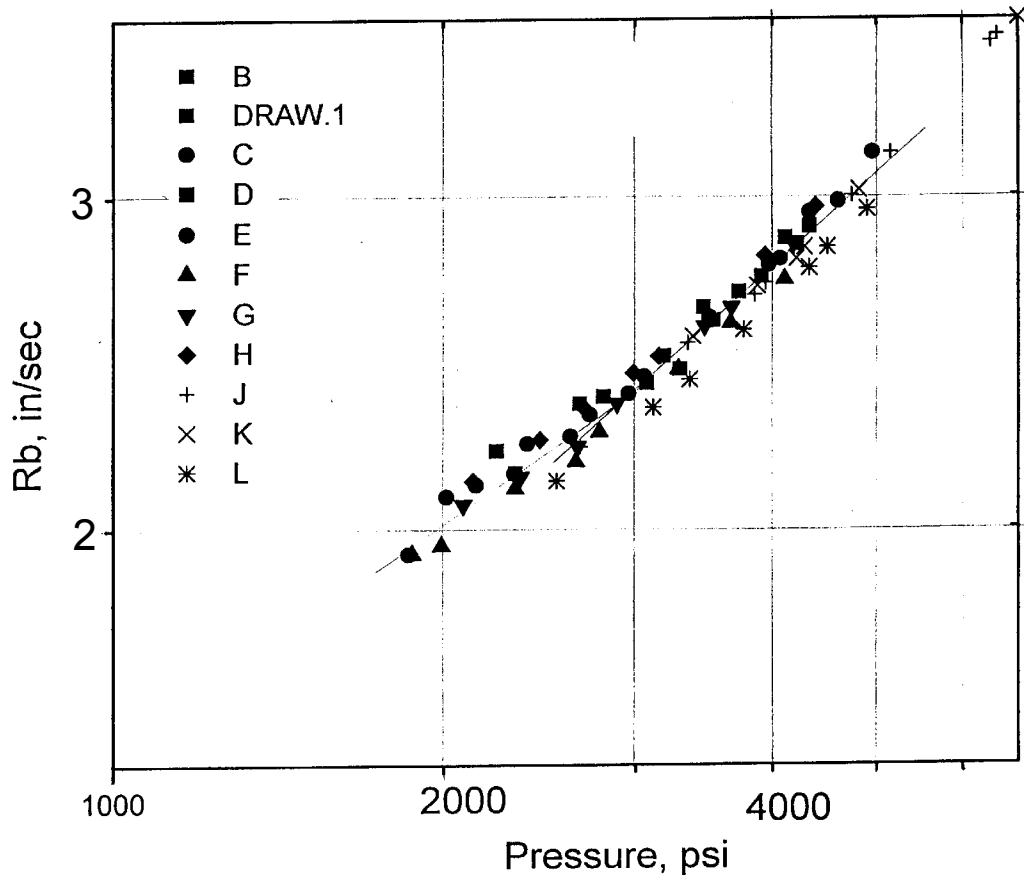


**Figure 2 Burn Rate Data for AP/HTPB Propellant with Catocene**

Many small SRM's have high propellant volumetric loading fractions for weight efficiency. For these motors, the port to throat area (ratio of the aft end propellant grain diameter to the throat area) is reduced driving the internal flow Mach Numbers upward. Thus, significant cross-flow velocities at the propellant surface are induced.

As the chamber Mach Number increases the resulting cross-flow velocity at the propellant surface results in heat transfer conditions that deviate considerably from the condition in the strand burner test. The burn rate experienced at a local static pressure condition in the full scale motor is greater than the strand burner data at the same pressure, and can be attributed to the increased heat transfer from the hot combustion gases in

cross-flow to the propellant [2]. This increase in burn rate, called erosive burning, can be clearly seen in full scale motor tests as shown in Figure 3.

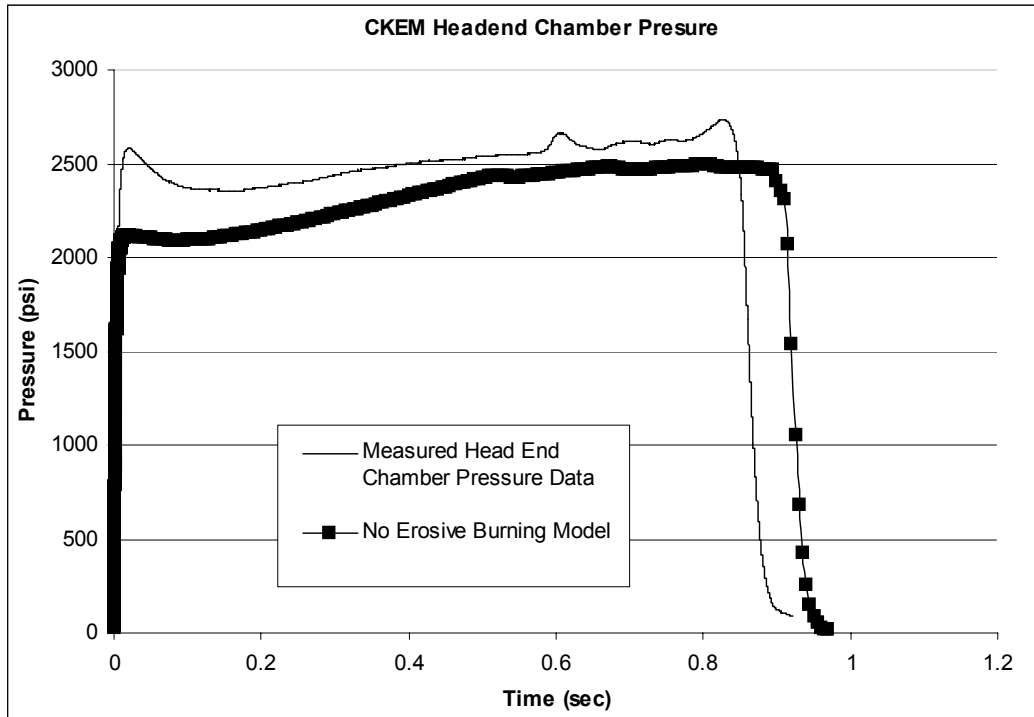


**Figure 3 CKEM Measured Chamber Pressure**

The figure shows two curves, one being the measured data, and the other being a prediction using a 3-D internal ballistics code with the burning rate of the propellant calculated with the equation  $r=cP^n$  calibrated to strand data. The measured pressure data shows a pressure spike at the beginning of the trace, which is characteristic evidence of erosive burning. Notice that the curves tend towards each other as time progress, which should be expected since the cross flow velocity at the burning surface decrease as the port opens as the propellant regresses back.

### 1.1 Problem Definition

Most SRM design codes have several engineering models available to account for erosive burning. The most widely used are as follows in order of Lenoir-Robillard [3], Green' Formula [4], Kriedler's Formula [5], and the exponential law.

$$r_e = r + \frac{\alpha G^{.8}}{D^{.2}} \exp(-\beta \rho_p r / G) \quad (1)$$

$$\begin{cases} r_e = r[1 + k(G / G^*)] \\ G^* = p \sqrt{\frac{\gamma}{RT}} \end{cases} \quad (2)$$

$$r_e = r[1 + k(G / p^{.485})] \quad (3)$$

$$r_e = rp^{(kM)} \quad (4)$$

All of the above equations, with the exception of Equation 4, contain empirical constants and constants specific to the actual SRM geometry or ballistics. Therefore these equations are not suitable for design prediction calculations, but must be calibrated to full scale motors operating at conditions very similar to the proposed SRM design.

Since erosive burning is a function of the internal gas velocities of a motor, the greatest effect is often seen as a pressure spike at start-up when the internal velocities are the highest. This spike is often the maximum pressure seen throughout the motor firing, and can drive the structural design of the motor. As such, the spike must be considered

early in the design process. The ability of an internal ballistics code to predict erosive burning based on limited data is critical. Given an accurate means of predicting erosive burning, the effects can be either accounted for in the initial design, or, more preferably, designed out of existence.

### *1.2 Erosive Burning Mechanisms*

Erosive burning is defined as the increase in burning rate of a solid propellant that occurs as a function of hot gas cross-flow at the propellant surface [6]. The amount of burning rate increase is established by comparing the erosive burning rate to the burning rate that occurs at the same local pressure for no cross-flow. The primary mechanism for the increase in rate is the additional heat that is fluxed into the surface as a result of the cross-flow. Several factors contribute to this increase in heat flux, including the thermal gradient in the boundary layer, and turbulent enhancement of the local transport properties.

As the free stream flow velocity is increased over the burning propellant, the boundary layer is compressed. Thus, the temperature gradient at the surface of the propellant is increased which results in an increase in heat transfer to the surface. Although the pyrolysis of a composite propellant is complex in that several constituents outgas from the surface at different melt temperatures, the net activation energy of the pyrolysis process is very high; thus, small changes in temperature result in large increases in pyrolysis rates. The pyrolysis process acts similar to a simple melt process; thus, the increase in energy flux to the surface is balanced by an increase in the pyrolysis rate, as opposed to a substantial increase in the surface layer temperature (the surface layer refers

to a thin layer near the propellant surface composed mostly of unreacted APd and binder gas).

The second mechanism that contributes to erosive burning is the increase in local transport properties due to turbulent fluctuations. The primary effect of turbulence is to increase the apparent thermal conductivity, and thus increase the heat flux from the hot free stream combustion gases through the boundary layer to the surface. A secondary effect is an increase in the mixing rate of the APd and binder diffusion flame. Finally, the stand-off distance of the flame front from the burning surface is influenced by cross-flow. As the boundary layer compresses, the near wall gas temperature increases which results in higher reaction rates.

### *1.3 Literature Review*

Several analytical studies of erosive burning have been conducted. Razdan and Kuo [7] used a turbulent boundary layer approach to show that the augmented burning rate with free stream velocity is due to the increased heat feedback and increase in transport coefficients, as well as increased turbulent mixing. Gordon, Duterque, and Lengelle [8] used a 1-D wall zone model coupled with a fully turbulent 2-D description of the whole flow field to develop an erosive burning model correlated to wall shear stress. They also concluded that the propellant's normal burning rate was the primary influence on the threshold for erosive burning. Bulgakov, and Karpov [9] also used the boundary layer equations to study the burning of stick propellant and negative erosive burning (a decrease in burning rate with blowing across the surface), and found satisfactory agreement with experimental data. King [10] conducted a very extensive survey of experimental methods, as well as numerical techniques and correlations. He classified

the most widely used models into three primary areas as follows: 1) those based on augmented heat transfer from the core flow, 2) those based on alteration of transport properties in the region between the flame zone and the propellant surface, and 3) models based on chemically reacting boundary layers. He also developed a “Second Generation” model built on a zero cross-flow composite propellant burning model which includes two mechanisms for burning rate augmentation, including the bending of a columnar diffusion flame by the cross flow, and the mixing and heat transport augmentation by cross flow induced turbulence. An eddy viscosity model was used for closure in the boundary layer analysis.

Most recently, Mukunda and Paul [11] conducted a study to examine the universal behavior of erosive burning. They completed a thorough review of the available data and correlations, and postulated that the effects of erosive burning were contained in two parameters,  $\eta$  and  $g$  in the following form:

$$\begin{aligned}\eta &= f(g_o \text{Re}_o^m) \\ g_o &= G / (\rho_p r_o) \\ g &= K_2 g_o \text{Re}_o^m\end{aligned}\tag{5}$$

They concluded that for most practical propellants, erosive burning effects are primarily a function of the non-erosive mass flux and the Reynolds Number, with little effect due to chemical kinetics. Yang et al. [12] have used LES to study solid propellant combustion in cross flow, and showed turbulent mixing dominates over chemistry.

#### *1.4 Opportunity for DNS*

Previous numerical work in erosive burning has not attempted to resolve both the flame zone and the near wall flow structures which dominate the erosive burning problem.

A unique opportunity for DNS exists because it provides an accurate means of resolving all relevant scales in the erosive burning problem. As the literature shows, the primary mechanisms involved in erosive burning are the cross-flow augmented heat transfer from the flame front to the burning surface, and an energy balance at the solid–gas interface. This thesis describes the results of using DNS to analyze the primary mechanisms that govern the erosive burning, including chemical reactions, and presents an approach for using the DNS results for a practical engineering application. A high rate AP/HTPB propellant which has considerable strand burn rate data, and full scale motor data available, is chosen for the analysis. Two approaches are presented. The first is a heat transfer based model that incorporates an infinite rate chemistry model. Secondly, a two-step, global, finite rate chemistry model and Arrhenius pyrolysis law are used. Both approaches are calibrated to strand burn rate data by modeling a quiescent environment using DNS. Subsequent DNS calculations are made where cross-flow is induced from  $M=0.0$  to  $M=0.8$ . The increased regression rate with Mach Number, and the resulting flame structure (finite rate model only) are studied.

The results of the DNS analysis are incorporated into a fully 3-D interior ballistics code and used to predict the chamber pressure of a motor known to have extensive erosive burning. The purpose of this step is to evaluate the magnitude of the DNS predicted rate increase due to cross-flow as compared to the base burn rate. The DNS results are incorporated in the ballistics code in the following way:

$$r_e = r \left( \frac{r|_M}{r_o} \right) \Big|_{DNS} \quad (6)$$

The local burn rate,  $r$ , is calculated using  $cP^n$ , and then adjusted upward based on the local Mach Number, and the ratio predicted through the DNS analysis.

### *1.5 Summary of Content*

In Section 2, the DNS code developed for this study is described, including the numerical schemes, boundary conditions, and verification process. Section 3 contains a brief description of the internal ballistics code used in the study. In Section 4, the DNS calculations and developed erosive burning models are presented, along with the internal ballistics calculations using the models. The final section contains the conclusions drawn from the study with a recommendation on the most accurate, but efficient means of developing an erosive burning model using DNS.

## CHAPTER 2

### PRESENTATION OF OBJECTIVES

#### *2.0 Overview of Objectives*

The primary objective of this work is to demonstrate an approach for developing a DNS based erosive burning model for a given propellant that can be incorporated into an SRM interior ballistics design code. To be a useful design tool, the model must be shown to predict accurate results while relying only on information that would be available to the design engineer during an initial rocket motor design phase. This information includes a detailed propellant formulation, theoretical thermochemical analysis, and propellant strand burn rate data. The objectives are as follows:

#### *2.1 Objective-1 Develop a Calibrated DNS Computer Code.*

The primary physical mechanisms influencing erosive burning are heat transfer in a turbulent boundary layer, and the position of the flame fronts in relation to the burning surface. DNS analysis provides a means of accurately modeling the erosive burning problem by resolving the turbulent and chemistry scale. A DNS code is developed using an extended MacCormack [13] approach giving second order time, and fourth order space accuracy. Grid stretching is used to concentrate the computational grid in the vicinity of large flow and species gradients. The DNS code is verified by resolving a flow field with an accepted solution, namely, low Reynolds Number Poiseuille flow.

## *2.2 Objective-2 Infinite Rate Chemistry Erosive Burning Model*

To isolate and examine the individual contributions to erosive burning that the flow field and the combustion process make, the initial DNS calculations are made using an infinite rate chemistry model. The infinite rate chemistry model assumes all chemical reactions occur instantaneously above the propellant surface. The literature shows that the primary mechanism in erosive burning is increased heat transfer through the compression of the boundary layer as the Mach Number increases. A high rate AP/HTPB propellant with strand burn rate data is used to calibrate the analysis. DNS calculations are run for a range of Mach Numbers of  $M=0.0$ ,  $0.1$ ,  $0.5$ , and  $0.8$ . The  $M=0.0$  case is used to calibrate the pyrolysis of the propellant to the strand data. Since infinite rate chemistry is used, the propellant surface temperature is assumed, based on typical values seen in other analyses, and is held constant for all Mach Numbers.

## *2.3 Objective-3 Examination of Constant Surface Temperature Assumption*

As the burn rate increases with Mach Number and the heat transfer rate at the surface is increased, the propellant surface temperature should rise. Since the infinite rate chemistry assumption used in Objective 2 does not accurately predict the surface temperature, it is assumed constant. To investigate the impact of this assumption, a DNS calculation is made at a cross-flow  $M = 0.1$ , where the surface temperature is calculated based on an energy balance at the surface, and a pyrolysis law [14] of the form

$$r = r_o \exp \left[ \frac{E_a}{R_u} \left( \frac{1}{T_{surf_o}} - \frac{1}{T_{surf}} \right) \right] \quad 7)$$

-where  $r_o$  is the  $M=0.0$  burn rate, and  $T_{surf_o}$  is the surface temperature assumed in Objective 2. The resulting temperature, and the resulting burn rate are compared to the values obtained at  $M=0.1$  in Objective 2.

#### *2.4 Objective-4 Interior Ballistics Analysis*

The DNS infinite rate chemistry results are plotted and curve fit as  $r/r_o$  versus Mach Number, where  $r/r_o$  is the erosive burn rate at a given Mach Number, and  $r_o$  is the base burn rate ( $M=0.0$ ). The model is incorporated into a 3-D interior ballistics computer program, and used to predict the pressure of a U.S. Army tactical SRM for which static test data is available, and in which erosive burning is known to exist.

#### *2.5 Objective-5 Thermal Boundary Layer Growth Impact*

Since one of the primary mechanisms of the erosive burning problem is heat transfer from the free stream to the propellant surface, the thermal boundary layer profile boundary condition may influence the results. In both the finite and infinite rate chemistry model developments, a fully developed turbulent velocity profile is prescribed at the entrance of the computational domain. The thermal profile matches the velocity profile through compressible flow relationships. The width of the burning propellant is set to approximately 2% of the computational domain. Adiabatic walls are assumed from the entrance to the burning propellant. To investigate the impact of this assumption, one DNS run is made at a cross flow Mach Number of  $M=0.1$ , where the width of the propellant strip is increased to 50% of the bottom width. The change in burn rate as a function of location along the propellant surface is compared for the two cases.

### *2.6 Objective-6 DNS Model Universalism*

To demonstrate the universalism of the developed model, a second interior ballistics analysis is conducted on a motor that contains the same propellant as the one previously analyzed, but cast into a different configuration. This configuration has a different flow field, and operating pressure than the previous. The level of erosive burning is effected by the change in configuration. The primary purpose of this analysis is to show that the DNS generated erosive burning model is not highly dependent on the full scale motor geometry. By showing that the model is calibrated to individual propellant characteristics, as well as being loosely dependent on full scale geometry, the approach can be considered to be universally applicable to other rocket motor designs.

### *2.7 Objective-7 Finite Rate Chemistry Model.*

The position of the flame front in relation to the burning surface is expected to be effected by the cross-flow velocity. As such, the heat feedback from the flame to the propellant surface should be a function of the free stream Mach Number. To examine this mechanism, a two-reaction, global finite rate chemistry model is incorporated into the DNS calculations. In the finite rate chemistry model, chemical reactions take place over a finite time and distance via a rate equation. The two reactions considered are the exothermic AP decomposition reaction, and the premixed decomposed AP and HTPB reaction. In this analysis, the surface temperature is not assumed, but calculated for each case. The pyrolysis rate for the  $M=0.0$  analysis is set to match the strand burner data. Using the calculated surface temperature as the reference temperature in the exponential pyrolysis law shown in Equation 7, subsequent DNS runs are made at  $M=0.1$  to compare to the infinite case.



## CHAPTER 3

### DNS COMPUTER CODE DEVELOPMENT

#### *3.0 Introduction*

Numerical analysis of solid propellant combustion is unique in that the regression rate of the propellant is ultimately determined by an energy balance at the moving interface between a solid and a gas. High resolution of both the gas and solid at this interface is critical. In addition, composite solid propellants are self oxidizing in that they are mixtures of oxidizer, fuel, and minor ingredients. In general, this produces multiple flames that are positioned close to the surface. Rate equations for both the pyrolysis process and the combustion chemistry are required.

DNS also has several unique requirements. Because the computational domain is in general a very small part of a much larger flow field, the application and representation of the gas boundary conditions requires unique relationships, such as characteristic wave boundaries. Also, the specific problem may require the ability to vary or iterate on select variables to obtain the desired solution. Consequently, the development of a problem specific computer code is often more efficient than the adaptation of a general purpose combustion code.

Presented in this section is the DNS computer code that has been developed for the study of the erosive burning problem. Although this tool can be applied to many two dimensional DNS type flow fields, the organization of the input, output, gridding, boundary conditions, etc., is convenient for the study of the erosive burning problem.

### *3.1 Overview of DNS Code*

In DNS analysis, all fluid and chemistry structures are resolved down to the resolution of the grid; thus there is no need for the assumption of laminar or turbulent flow. However, grid resolution must be carefully considered. The conservation equations are solved directly with no need for subscale modeling of turbulence or mixing. A fully compressible, 2-D, finite differencing DNS code has been written based on an extended MacCormack scheme [13]. Grid stretching is utilized in the analyses by stretching in all directions away from the propellant surface to assure high resolution in the regions of large gradients. Characteristic boundary conditions are applied at the inlets and outlets. Conduction in the solid propellant is calculated with a second order central scheme. Surface energy balance derivatives are calculated using second order forward and backward schemes. Accuracy of the code is demonstrated by calculating Poiseuille flow in a channel.

### *3.2 Governing Equations*

The governing equations that are solved in the DNS analysis of the erosive burning problem are the conservation of mass, momentum, and energy, as well as the ideal gas equation of state. With the inclusion of finite rate chemistry, the conservation of species and the caloric equation of state are required. The conservation equations are listed below in order of the conservation of mass, momentum, energy, the ideal gas equation of state, the conservation of species, and the caloric equation of state:

$$\left\{ \begin{array}{l} \partial_t \rho + \partial_i (\rho u_i) = 0 \\ \partial_t (\rho u_i) + \partial_j (\rho u_i u_j) = -\partial_j p \delta_{ij} + \partial_j \tau_{ji} \\ \partial_t (\rho E) + \partial_i (\rho u_i E) = -\partial_i q_i - \partial_i (p u_i) + \partial_j (\tau_{ji} u_i) \\ p = \rho \frac{R_u}{MW} T \\ \partial_t (\rho Y_m) + \partial_i [\rho Y_m u_i + \rho V_{i,m} Y_m] = \rho \dot{\omega}_m, \quad m=1, N \\ h_m = \Delta h_{f,m}^\circ + \int_{T_o}^T c_{p,m}(T) dT \end{array} \right. \quad (8)$$

The heat flux vector,  $q_i$  is expressed in Fourier's form as

$$q_i = -k_g \partial_i T \quad (9)$$

where  $k_g$  is the conductivity of the gas. The viscous stress tensor  $\tau_{ij}$  is expressed as

$$\tau_{ij} = \lambda \partial_k u_k \delta_{ij} + 2\mu S_{ij} \quad (10)$$

where

$$S_{ij} = \frac{1}{2} (\partial_j u_i + \partial_i u_j) \quad (11)$$

and  $\lambda$  is taken as  $(-2/3)$  for a diatomic gas.

Thermochemical equilibrium calculations (NASA-Lewis Code) [15] are made at the chamber conditions to find  $\mu$  and the Prandtl Number ( $Pr$ ). The conductivity is then calculated as

$$k_g = \frac{c_p \mu}{Pr} \quad (12)$$

where the gas specific heat and molecular weights are also derived from the equilibrium calculations. All properties are calculated at the applied pressure boundary condition used in the DNS calculations.

### 3.3 Gas Phase Boundary Conditions

The computational domain considered is a portion of a 2-D channel with the burning propellant located at mid-center on the bottom wall. Following the work of Poinso and Lele [16], characteristic boundary conditions are prescribed at the domain's inlet and outlet. The solid bottom wall is treated as a no-slip surface, and the inlet and outlet are treated as non-reflecting, subsonic boundaries. Since the propellant is assumed to be burning in fully developed turbulent flow, the prescribed inlet velocity profile enforces this condition. The inlet and walls are given an initial and constant chemical composition. The burning propellant is assumed to flux gas at a fixed chemical composition into the fluid computational domain.

The inlet fluid is assumed to be combustion products at a stagnation temperature equal to the adiabatic flame temperature of the propellant. For each DNS calculation, the inlet free stream Mach Number is set, thus the free stream static temperature is calculated as

$$T_{\infty} = T_o / \left(1 + \frac{\gamma-1}{2} M_{\infty}^2\right) \quad (13)$$

from which the free stream velocity is calculated as

$$U_{\infty} = M_{\infty} \sqrt{\gamma R T_{\infty}} \quad (14)$$

The turbulent inlet velocity profile is based on fully developed channel flow with integral scale dimensions equal to the combustion chamber of the full scale motor which is later used in the interior ballistics analysis. The velocity profile is shown in the Appendix in Figure 48. The temperature profile is set based on the free stream velocity as

$$T_{ij} = T_o - (u_{ij}^2 + v_{ij}^2)/(2C_p) \quad (15)$$

where the  $i$ - $j$  indices represent the local conditions at the inlet.

The outlet characteristic boundary condition is set as a non-reflecting subsonic outlet. This condition assumes constant pressure at infinity, with the pressure at the outlet adjusted by characteristic waves that are assumed to propagate from the constant pressure reservoir at infinity.

The boundary condition at the top of the domain sets the slope of the normal velocity component to zero. The implication of this boundary condition is that the normal velocity component fluctuations are assumed to relax to negligible values toward the top of the domain. This is assumed valid since the domain is located above a  $y^+$  value of 75 for all cases.

### *3.4 Thermal Transport Model*

The rate at which the propellant burns is dependent on an energy balance at the solid to gas interface. Therefore, a thermal transport model which accurately establishes the temperature gradient at the surface, and thus the conduction into the solid, must be used. The energy equation for the solid reduces to

$$\rho_p C_s \partial_o T = \partial_i (k_s \partial_i T) \quad (16)$$

The conductivity [17], specific heat, and density of the solid propellant are assumed to be spatially invariant, thus the RHS of the equation converts to a second derivative of temperature, and is solved with a second order central differencing scheme. The propellant density is the theoretical density for the subject propellant, and  $k_s$  [17], and  $C_s$  are established by the mass ratio of AP to HTPB in the CKEM propellant, assuming the minor ingredients are insignificant in mass fraction (AP + HTPB  $\sim$  95% of the total mass for the assumed propellant). During the solid propellant's cure cycle, some shrinkage occurs, but this is assumed to have an insignificant effect on the theoretical value of  $\rho$ .

The regression of the propellant will impact the temperature gradient in the solid at the surface. To account for this without moving the solid grid, the thermal transport equations are adjusted to account for a moving reference frame, based on the local burn rate. The propellant is assumed to be fed into the combustion chamber at the rate the propellant is burning. The bottom of the propellant is held at ambient temperature, and the heat flux through the solid in the transverse direction is adjusted by interpolating the temperature solution in the solid upward by a distance of  $rdt$  after each time step. The term accounts for the energy deficit that is carried forward by the cold propellant.

### 3.5 Gas-Solid Interface

In this analysis, radiation from the gas to the surface is not considered directly, but is indirectly accounted for by the adjustment of the gas thermophysical properties to match test data; thus, the energy balance equation used is of the form

$$q_{g_{con}} = q_{p_{con}} - QM \quad (17)$$

or in expanded form

$$k_g \partial_i T = k_s \partial_i T - Q\mathbf{M} \quad (18)$$

where  $\mathbf{M}$  is the mass flux from the burning propellant, and can be related to the burn rate or pyrolysis rate as  $\rho_p r$ . Cazan and Menon [17], and others [14] have incorporated a model of the form

$$r = A \exp\left(\frac{-E_a}{R_u T_{surf}}\right) \quad (19)$$

to relate the surface pyrolysis rate to the propellant surface temperature. Using typical values for the activation energy of AP and HTPB [17], Equation 19 can be used to predict the propellant's burning rate if the surface temperature is known. In this study, and in most conceivable situations, the base burning rate is measured and known as a function of pressure ( $r = \rho_p c P^n$ ), but the surface temperature and the pre-exponential factor are not.

To find the pre-exponential factor in Equation 19, the pyrolysis equation can be forced to match a reference regression rate at some reference surface temperature. Using  $r = cP^n$  as the reference regression rate, the constant  $A$  can be shown to equal

$$A = \frac{cP^n}{\exp\left(\frac{-E_a}{R_u T_{surf_o}}\right)} \quad (20)$$

Substitution of Equation 20 into Equation 19 results in an equation that describes the regression of the propellant at surface temperatures above the reference condition.

$$r = cP^n \exp\left[\frac{E_a}{R_u}\left(\frac{1}{T_{surf_o}} - \frac{1}{T_{surf}}\right)\right] \quad (21)$$

Equation (21) is incorporated into the surface energy balance equation, which is solved within each time step for the unique value of  $T_{surf}$ , given a value of  $T_{surf_o}$ . The velocity of the gas injected from the burning propellant is calculated from a mass balance at the surface as

$$\rho_p r = \rho_p v_{norm} \quad (22)$$

where  $v_{norm}$  is the gas velocity normal to the propellant surface.

### 3.6 Numerical Schemes

The governing equations in the fluid domain are solved using a MaCormack [18] scheme. The basic scheme is an explicit, time marching scheme that produces second order time and space accuracy. The time derivative at each time step is first calculated by calculating the spatial derivatives with a first order forward scheme. The solution is temporarily advanced in time, where the time derivatives are then recalculated based on the new values and a first order backward scheme. The two time derivatives are averaged, and the solution is permanently advanced one time step. The scheme can be written symbolically [19] as:

$$\begin{aligned} \bar{u}_i^{n+1} &= u_i^n - c\Delta t \frac{u_{i+1}^n - u_i^n}{\Delta x} \\ u_i^{n+1} &= \frac{1}{2} \left( u_i^n + \bar{u}_i^{n+1} - c\Delta t \frac{u_i^{\bar{n}+1} - u_{i-1}^{\bar{n}+1}}{\Delta x} \right) \end{aligned} \quad (23)$$

where  $n$  is the time step, and  $i$  is the spatial location index. The forward and backward differencing steps are alternated between successive time steps to prevent a biased

solution. The scheme can be extended to fourth order spatial accuracy by replacing the first order forward and backward terms with second order forward and backward schemes.

The above illustration of the MaCormack scheme shows only first order or convection terms. The momentum, energy, and conservation of species equations contain second order diffusion terms as well. These terms are spatially differenced with second or fourth order central differencing schemes, depending on the user's selection. These terms are also calculated twice within each solution time step, and contribute to the averaged time derivative.

### 3.7 Code Verification

To verify the DNS code, including the characteristic boundary conditions, a low Reynolds Number compressible, channel flow problem is analyzed. The computational domain consists of a channel with a length to half width ratio  $L/l=10$ . The inlet Mach Number is set to  $M=0.1$ , with an inlet velocity profile described as [16]:

$$\begin{aligned} u_1(0, x_2, t) &= u_o \left[ \cos\left(\frac{\pi x_2}{2l}\right) \right]^2 \\ u_2(0, x_2, t) &= 0 \\ T(0, x_2, t) &= T_o \end{aligned} \quad (24)$$

The exact solution for Poiseuille Flow between infinite channels is

$$u(y) = \frac{1}{2\mu} \frac{\partial p}{\partial x} (y^2 - l^2) \quad (25)$$

where  $l^2$  is the half-width of the channel. In the verification analysis,  $\mu=.3694 Pa\cdot s$ , and  $l=.01 m$ . As Figures 5-8 show, the DNS solution converges to a constant pressure drop of  $\frac{\partial p}{\partial x} = -88822.3 Pa/m$ , and a maximum center-line velocity of  $u(0)=12.019 m/s$ . The

exact solution for the given pressure drop is  $u(0)=12.023 \text{ m/s}$ , which gives an error equal to .03%.

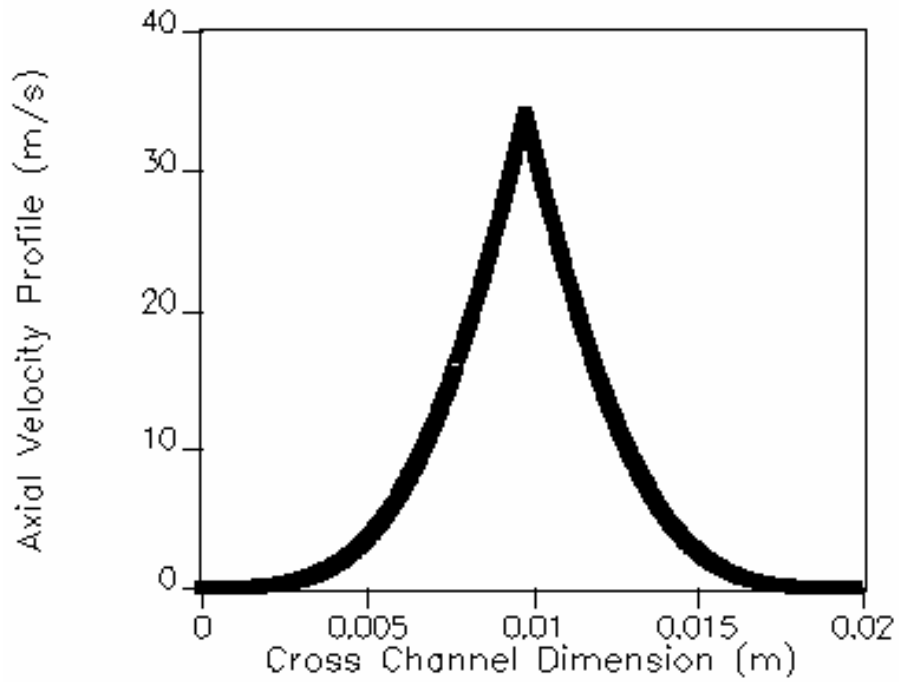


**Figure 4 Entrance Axial Velocity Profile (m/s)**

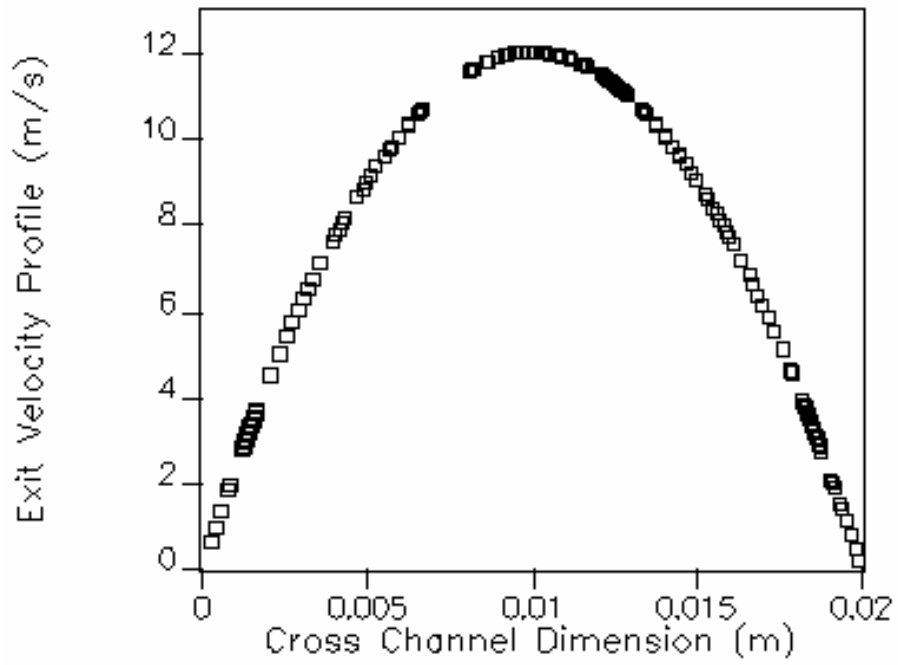


**Figure 5 Converged Exit Velocity Profile (m/s)**

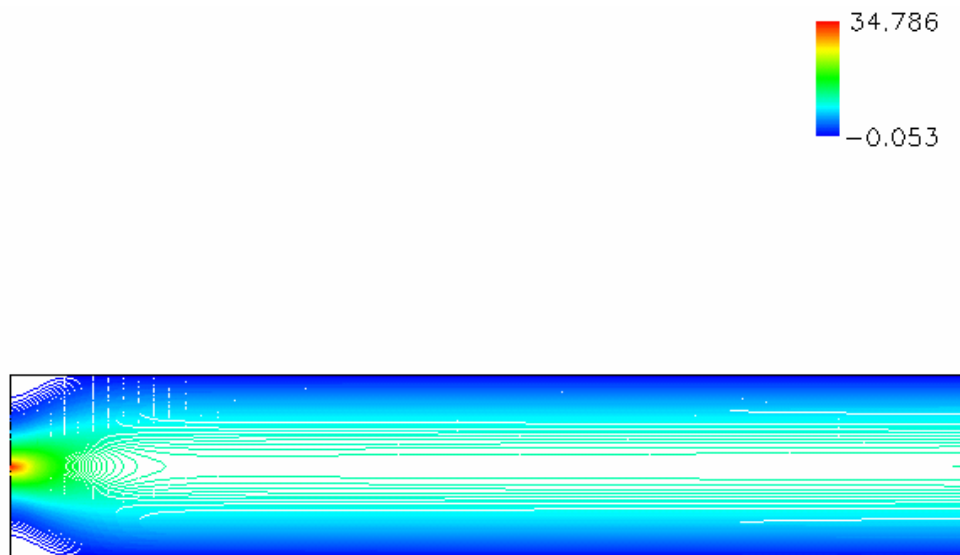


**Figure 6 Axial Velocity Contours (m/s)**

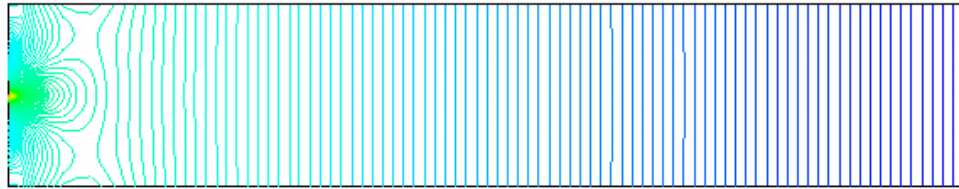
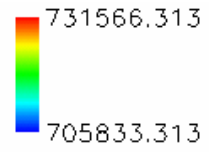


**Figure 7 Pressure Contours (Pa)**

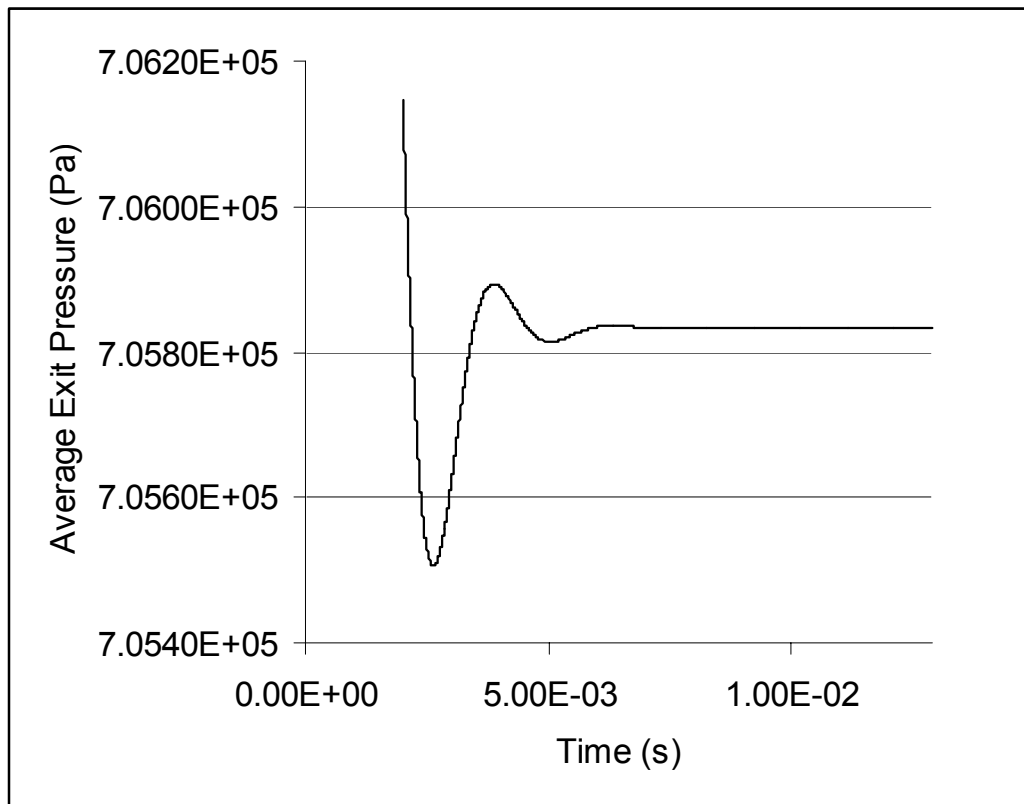


**Figure 8 Convergence History of Exit Pressure**

## CHAPTER 4

### INTERIOR BALLISTICS CODE DESCRIPTION

#### *4.0 Introduction*

The objective of interior ballistics analysis is to accurately predict the performance of a solid rocket motor for design and analysis purposes. In general, most solid rocket motor designs require moderate to high resolution of the flow field in the axial direction, with little resolution requirements in the circumferential direction. Modeling the regression of the propellant is required to capture the change in the combustion chamber volume and accurately predict the motor pressure with time. Because the objective of these design tools is to predict the complete time history of a motor firing (ranging in time from a few milliseconds to one minute or more) modeling the combustion process would require the consideration of time scales that would be prohibitive in total computer run time, and would not be a useful or efficient tool during a design phase where many geometry iterations may be required. Consequentially, the combustion process is treated as a mass and energy flux boundary condition with rates that are empirical in nature and are generally based on local flow variables such as pressure, axial mass flux, and axial velocity. Erosive burning is an additional feature that an interior ballistics code and design engineer must consider. However, erosive burning must also be modeled or empirically treated at the motor design level for efficiency.

Presented in this section is a proven interior ballistics code which has been successfully applied to many actual solid rocket motors. This code is used to implement the results of the DNS erosive burning analyses which will be presented in later chapters.

The inclusion of the use of this code shows a vital link between the highly resolved, small scale DNS analysis and a full scale practical design application.

#### *4.1 Overview of the Interior Ballistics Code*

The interior ballistics code used in this study, called 3DGE, was developed by Stone Engineering Company [20] for the United States Army Aviation and Missile Command. The objective of the code development was to provide a means of accurately predicting the rocket motor performance parameters of high burn rate, high internal Mach Number, short burning motors. The code is unique in that it begins with a 3-D finite element grid representation of the propellant geometry, which is regressed locally based on the local burning rate. An extensive library of burning rate models is available including the erosive burning models presented in Sec. (1). The code was first developed in 1995, and has been used extensively to successfully predict and/or simulate the ballistics of several U.S. Army solid rocket motors.

#### *4.2 Governing Equations*

The governing equations for the 3DGE ballistics code represent a compressible, inviscid, and 1-D flow field. Infinite rate chemistry and a single species working fluid are assumed, thus conservation of species is not required. The 1-D mass, momentum, and energy equations are as follows:

$$\begin{aligned}
\partial_t(\rho A) + \partial_1(\rho UA) &= \dot{m}_{gx} \\
(\rho A)\partial_t U + (\rho UA)\partial_1 U + U\dot{m}_{gx} &= -A\partial_1 P \\
\partial_t(\rho e_o) + \partial_1\left[\rho U\left(e_o + \frac{P}{\rho}\right)\right] &= \dot{m}_{gx}c_p T_G
\end{aligned} \tag{26}$$

In the above equations,  $\dot{m}_{gx}$  is the mass flux from the burning propellant,  $A$  is the control volume cross sectional area,  $P$  is the pressure,  $\rho$  is the density,  $U$  is the axial velocity, and  $e_o$  is the total energy of the gas. The mass is assumed to be injected normal to the flow direction at the adiabatic temperature of the combustion gases.

The flow field boundary conditions are based on Mach Number. The head end of the motor is assumed to have a Mach Number of  $M=0.0$ , while the aft end condition changes with time. Isentropic flow is assumed between the last burning station in the finite element grid point and the throat. The Mach Number boundary condition at the last burning station is calculated from the instantaneous subsonic, isentropic flow relationship between the burning station and the throat. The lateral boundary conditions are mass injection and moving walls corresponding to the local burn rate.

#### 4.3 Solution Methodology

The initial step in the solution process is to build a table of local flow area and circumference versus the local burn distance of the propellant. Thus, if the local total burn distance is known, then from the table, the local flow area and circumference can be interpolated. The initial burning propellant surface of the finite element grid is identified with a flag, such that an algorithm can be used to evaluate all internal geometry points of the propellant, as defined by the finite element grid. The algorithm calculates the normal distance from an interior point to the initial burning surface, which represents the distance the propellant must burn to uncover that point. The grid is divided into equally spaced

axial stations, where the interior points are stitched together to form a cross sectional flow area for a given burn distance and axial location. This procedure is shown schematically in Figure 9, where a cross section of propellant is shown. The schematic shows the initial burning surface, and a dashed line representing the connection of points moved in the plane a distance from the surface equal to the local burn distance. These areas are placed in a table for use in the ballistics code.

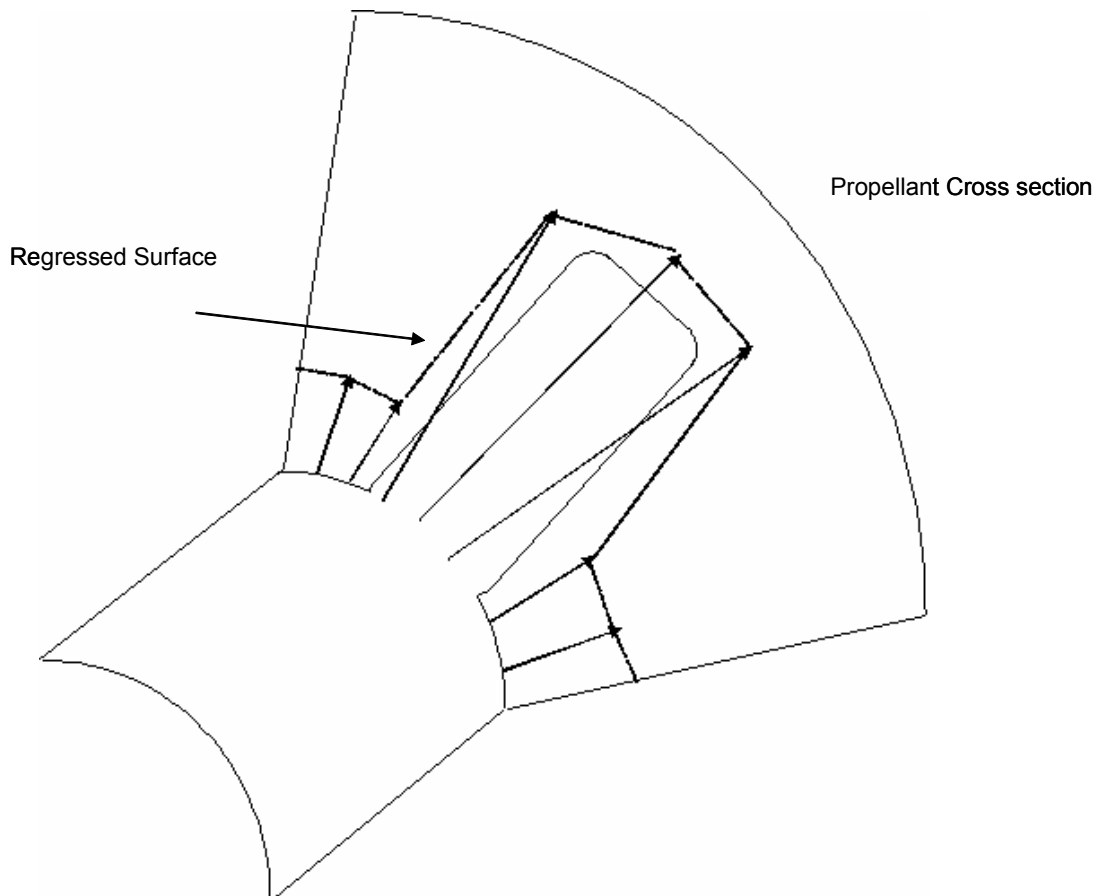


**Figure 9 Ballistics Code Regression Model Schematic**

The 1-D flow equations are solved explicitly in time using the Lax-Wendroff [27] scheme. The scheme can be represented as:

$$\begin{aligned}
 U_i^{t+\frac{\Delta t}{2}} &= U_i^t + \left( \frac{U_i^t - U_{i-1}^t}{\Delta x} \right) \\
 U_i^{t+\Delta t} &= U_i^t + \left( \frac{U_{i+1}^{t+\frac{\Delta t}{2}} - U_i^{t+\frac{\Delta t}{2}}}{\Delta x} \right)
 \end{aligned}
 \tag{27}$$

The scheme advances the solution a half time step using first order backward differencing. The time derivatives are again evaluated at the temporary solution using a forward scheme. The original solution is then advanced a full time step using the mid-step time derivatives. The resulting solution is second order accurate in time and space. The local conditions are used to calculate the local burn rate, which is then integrated in time to find the local burn distance. This distance is then used in conjunction with the geometry table to determine the local geometry.

#### 4.4 Code Verification

The 3DGE code was originally written to analyze a U.S. Army motor called AdKEM<sup>B</sup>. The motor is a fast burn motor, with HTPB/AP propellant. The initial aft end Mach Number boundary condition is  $M=1.0$  because the propellant grain is cast to the same diameter as the throat. Several static tests of the motor have been completed. Figure 10 shows a comparison of the simulation to an actual static test firing. As the figure shows, the agreement is excellent.

---

<sup>B</sup> AdKEM test data originated from Mr. Jerry Arzman - U.S. Army Aviation and Missile Command – Propulsion Laboratory, Huntsville, AL. 1995.

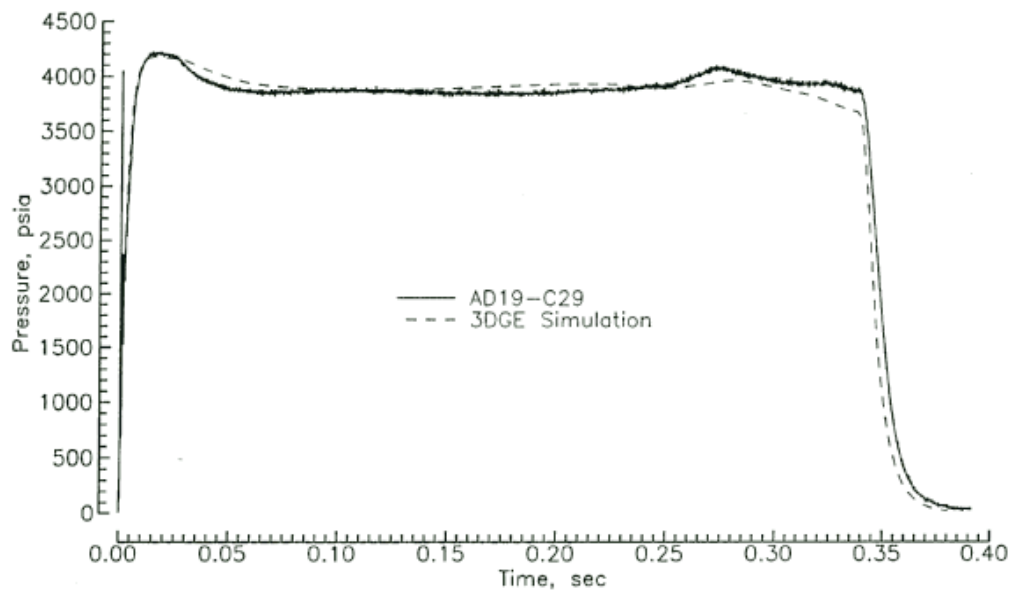


**Figure 10 Comparison of 3DGE to Static Test Data**

## CHAPTER 5

### EROSIVE BURNING NUMERICAL ANALYSIS

#### *5.0 Introduction*

In the development of a DNS erosive burning model that can be successfully implemented in an interior ballistics code, several logical steps must be followed. Of fundamental importance is the isolation and study of the primary controlling mechanisms of erosive burning (i.e. turbulent heat transfer and combustion chemistry). Resolution of the combustion zones generate the smallest time scale requirements. If chemistry can be shown to have a minor influence on the problem, then grid size requirements can be relaxed with a resulting reduction in computational time.

Secondly, sensitivity studies must be conducted to show that the results and conclusions are not dictated by artificial drivers, such as the choice of the computational domain size, or grid spacing. Similarly, the models must be calibrated to test data by the adjustment of certain thermophysical variables. However, the results must not be strongly dictated by the choice of the variables to adjust. The range of the application of the results must also be investigated. If the DNS model is centered around, and calibrated to a given chamber pressure and propellant base burn rate, the validity of these results in applications that deviate from these parameters must be established.

Finally, for the DNS model to be a useful tool for the design engineer and be considered an improvement to the current state-of-the-art interior ballistics analysis techniques, the models must be shown to accurately bridge the gap between subscale test data and full scale motor designs. As presented earlier, many erosive burning models

exist and adequately simulate rocket motor performance in designs that contain erosive burning. However, these models are strongly dependent on full scale motor dimensions, flow rates, etc. for calibration. Thus, these tools cannot be considered as predictive tools. The objective of the DNS approach is to show that an erosive burning model can be produced that is primarily dependent on propellant data (thermophysical properties, burn rate data, etc.), and is calibrated to subscale test data, with a weak dependence on the full scale parameters. This type of model can then be considered a predictive tool and useful in the initial design phase of a rocket motor.

This section presents the results of the DNS study of the erosive burning mechanisms, as well as sensitivity analyses to certain input variables. The generated models are then incorporated into an interior ballistic code to analyze the performance of an actual rocket motor, with a comparison to static test data.

### *5.1 Overview of Analysis*

The overall objective of this work is to use DNS to resolve the near wall region of a burning solid propellant, study the primary mechanisms that control erosive burning, and demonstrate the ability to develop an erosive burning model that is specific to a given propellant, and relies on limited initial design phase data. In addition, when incorporated into an internal ballistics analysis, the model should demonstrate the ability to accurately predict the performance of a solid rocket motor that is known to have significant erosive burning. The first approach is to develop the model assuming infinite rate chemistry. A finite rate analysis follows such that the flame structures and dependencies to cross-flow can be studied.

The fundamental assumption in developing the models is that closed bomb stand burn rate data is available for the subject propellant. An initial DNS calculation is made with no cross flow. The resulting propellant regression rate is calibrated to the strand data by varying certain thermodynamic properties, depending on the analysis, and used as a baseline for the cross flow cases. After the calibration step, the cross flow is increased in steps from  $M=0.0$  up to  $M=0.8$ , and the resulting regression rate, normalized by the base burning rate, is recorded as a function of Mach Number. The regression rate versus Mach Number curve is incorporated into the 3DGE ballistics code to calculate the performance of a motor configuration that has static test data available.

Several other analyses are conducted to demonstrate the sensitivity of the results to various input variables. These other cases include a comparison of a fixed surface temperature assumption to a floating temperature assumption, and a variation of the assumed propellant slab width (thermal boundary layer growth). The universalism of the model is demonstrated by applying it to a motor of different propellant geometry, but of identical propellant formulation. And finally, a finite rate model is developed for a low burning rate propellant to investigate the impact that the base burn rate has on the propellant's response to cross-flow.

## *5.2 Computational Domain*

The computational domain is considered to be a 2-D segment of a large 2-D channel having an integral scale based on the dimensions of the subject motor's combustion chamber. The domain dimensions are  $.1mm$  in the normal direction, and  $0.3mm$  in the stream-wise direction. Grid size requirements are determined by

$l_\eta = l_1 Re^{-3/4}$  giving a typical grid size requirement of  $1\mu m$  for  $M=0.1$ , down to  $0.25\mu m$  for  $M=0.8$ . The grid resolution is set at  $100 \times 300$  with a 20-1 stretch ratio in the normal direction. Figure 11 shows a schematic of the computational domain.

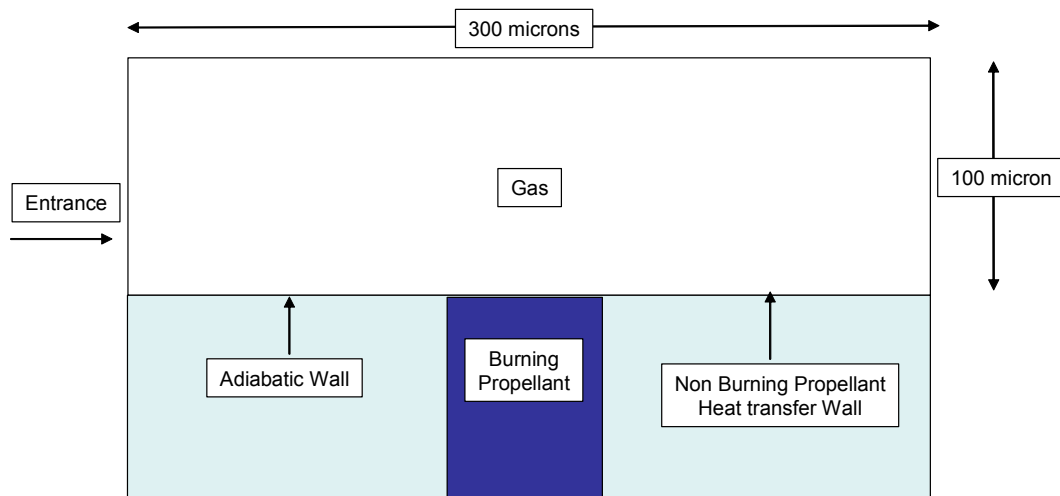


**Figure 11 Cross-Flow Computational Domain Schematic**

All computations are run on Pentium-4 machines. The analyses are run until the propellant surface temperature and/or the average regression rate converge to a statistically stable solution.

### 5.3.0 Infinite Rate Chemistry Model

To isolate the influence of the flow field on erosive burning from chemistry, the initial analysis that is performed uses an infinite rate chemistry model. Because of this assumption, this approach can be considered a heat transfer based model. As such, the calibration process will be to match the heat transfer from the gas to the solid at the solid-gas interface that results in a calculated regression rate that matches strand burn rate data. The primary assumption in this approach is that the heat release zone is fixed at the

propellant surface, and the mass flux from the surface is of combustion products only. The total energy (internal plus kinetic) of the combustion gases is set to the total energy of the adiabatic flame, based on thermochemical equilibrium calculations. The mass fraction of combustion gases is equal to one throughout the computational domain.

The objective of this study is to examine the increased rate of pyrolysis of the propellant as cross-flow is induced for a range of free-stream Mach Numbers. The boundary layer is expected to compress, increasing the temperature gradient at the wall, which will be countered by an increase in heat transfer into the solid, and an increase in the pyrolysis rate.

### *5.3.1 Rocket Motor Configuration*

To adequately evaluate the ability to develop a DNS erosive burn rate model, a configuration with sufficient test data is chosen. The U.S. Army's CKEM rocket motor, shown in Figure 12, contains a high rate HTPB/AP propellant, and has been statically tested in several configurations is chosen as the test case. Considerable strand burn rate data is available for this propellant. As the figure shows, the propellant grain is cast to the same diameter as the throat, thus the initial Mach Numbers will approach  $M=1.0$  at the aft end of the motor. The advantage of this test case is that the motor has been tested with the same propellant in different configurations, and thus gives opportunity to demonstrate the universalism of the erosive burning model generated through DNS.

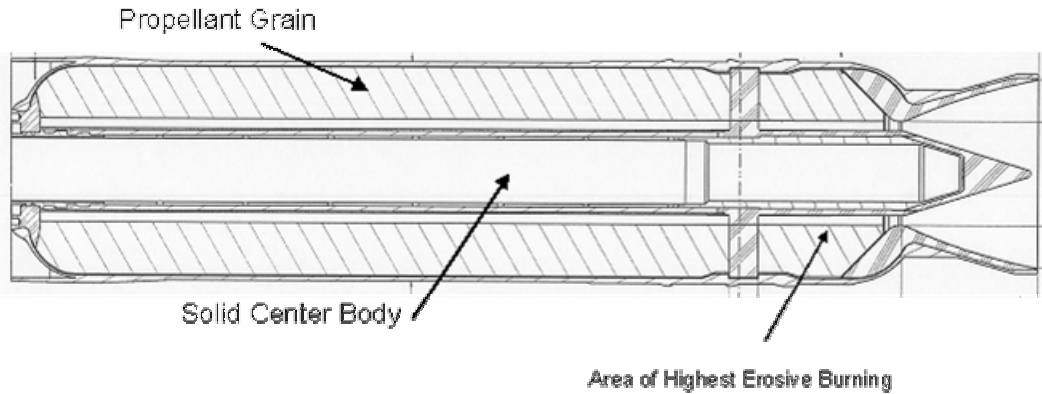


**Figure 12 CKEM Rocket Motor Schematic**

The propellant in the CKEM motor is an HTPB/AP propellant with a burn rate modifier to increase the rate. The strand burn rate data show that the propellant has a nominal burning rate of  $5.25 \text{ cm/s}$  at a pressure of  $17.24 \text{ MPa}$ . Thermochemical equilibrium analysis is used to calculate the adiabatic temperature, Prandtl Number, and other relevant thermodynamic properties. Since the HTPB and AP constitute approximately  $95\%$  of the total mass of the formulation, properties of the solid are calculated based solely on the ratios of these two ingredients.

Table 1 Physical Properties of The CKEM Solid Propellant and Combustion Gases

Physical Properties	Values
<i>Adiabatic Flame Temperature (<math>T_{ab}</math>)</i>	<i>3024 K</i>
<i>Prandtl Number (<math>Pr</math>)</i>	<i>0.58</i>
<i>Viscosity @ <math>T_{ab}</math> (<math>\mu</math>)</i>	<i><math>1 \times 10^{-4}</math> Pa-s</i>
<i>Solid Propellant Conductivity (<math>k_s</math>)</i>	<i>0.397 W/m-K</i>
<i>Solid Density (<math>\rho_p</math>)</i>	<i>1744 kg/m<sup>3</sup></i>
<i>Solid Specific Heat (<math>C_s</math>)</i>	<i>1256 J/kg-K,</i>
<i>Heat of Pyrolysis (<math>Q</math>)</i>	<i><math>13.62 \times 10^5</math> J/kg,</i>
<i>Pyrolysis Activation Energy (<math>E_a</math>)</i>	<i>21.12 kcal/mol</i>

### 5.3.2 Constant Surface Temperature Analysis

A series of DNS runs are conducted for a range of Mach Numbers of  $M=0.0-0.8$ , where the propellant surface temperature is assumed to stay constant, independent of the regression rate of the propellant. The validity of this simplifying assumption is based on Equation 19, which shows that for a large value of activation energy, the percent change in surface temperature with regression rate is very small. Therefore, when cross flow is introduced, and the heat transfer at the surface increases, the dominate effect is that the regression rate increases greatly, with small surface temperature changes.

The propellant surface temperature is fixed at a value of  $1143$  K, which is derived from the literature [14], in conjunction with Equation 21. The reference temperature is assumed to be  $835.0$  K at a reference burn rate of  $0.17$  cm/s. This reference temperature is used in this analysis as an estimate of the true surface temperature. Although the

reference case is for an HTPB/AP propellant, minor ingredient changes will change the pre-exponential factor, and thus change the surface temperature at any given rate. This is accounted for in the analysis by calibrating the regression rate to actual test data for the specific propellant in question through the adjustment of the heat of reaction. Thus the heat transfer is matched at the surface for a known test condition. For a base burn rate of  $5.25 \text{ cm/s}$  (the subject propellant at  $17.2 \text{ MPa}$ ), and an activation energy of  $21.12 \text{ kcal/mol}$  [17], the predicted surface temperature is  $1143.0 \text{ K}$ . The zero cross-flow condition is used to calibrate the energy balance at the propellant surface by finding a value for the heat of pyrolysis which gives the desired burn rate (CKEM strand burner data) at the assumed surface temperature.

Using the assumed surface temperature and heat of pyrolysis from the zero cross flow case, DNS runs are conducted at free stream Mach Numbers of  $M=0.1$ , and  $0.8$ . Using an energy balance at the propellant surface, based on the flow conditions at each Mach Number, a new regression rate is calculated. The DNS calculations are run until a steady, time average regression rate is achieved.

Using the steady time average regression rate obtained at each Mach Number, the function  $(r/r_o)$  is plotted versus Mach Number as shown in Figure 13.

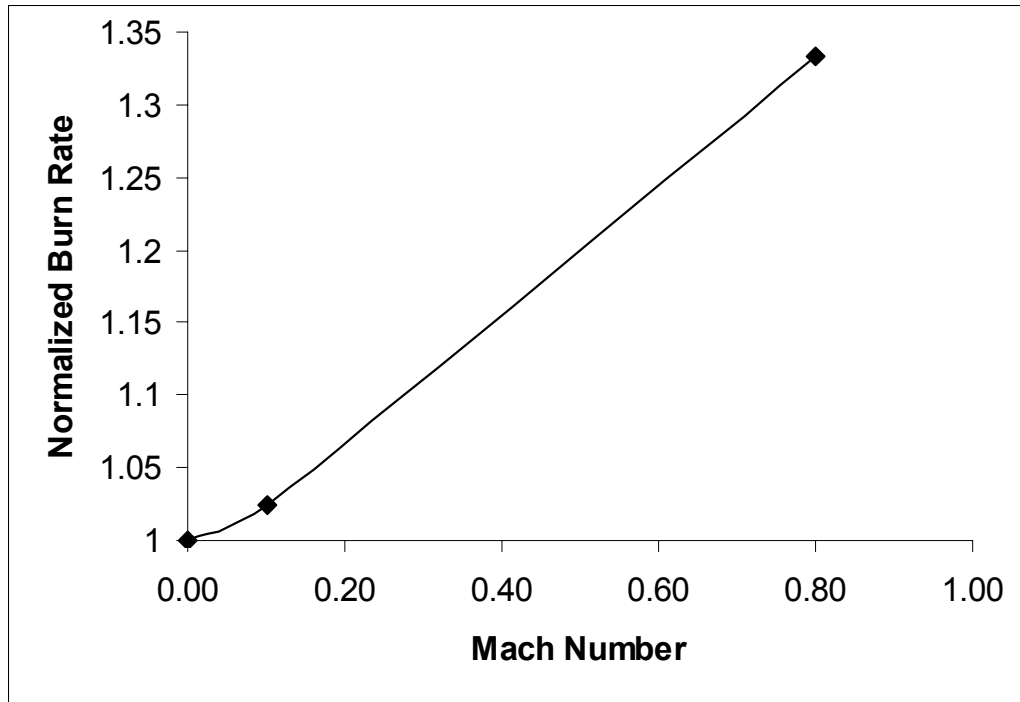


**Figure 13 Normalized Burn Rate versus Mach Number**

### 5.3.3 Ballistics Analysis Using the Infinite Rate DNS Model

The above data is curve fit linearly between points and incorporated into the 3DGE internal ballistics code using Equation 6. The local burn rate at each axial location in the grain is calculated using  $r=cP^n$ . The burn rate is then adjusted based on the local Mach Number, and the relationship shown in Figure 13. The resulting head-end pressure prediction shows excellent agreement and is shown in Figure 14.

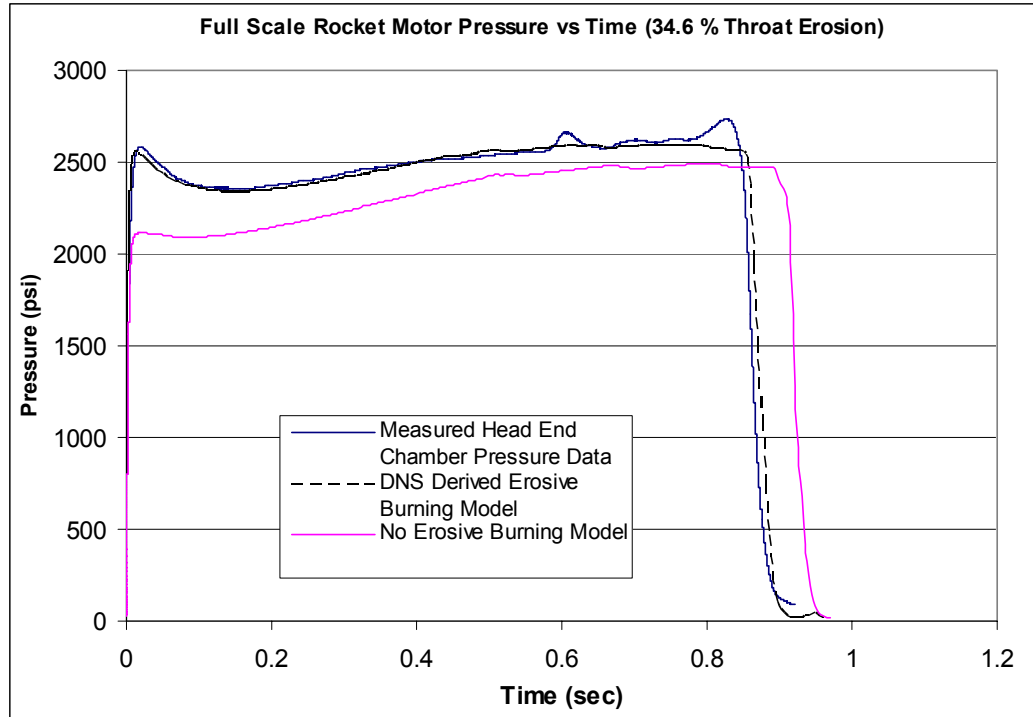


**Figure 14 Internal Ballistics Calculations Using DNS Results**

As Figure 14 shows, the DNS model shows excellent results in light of the assumption of constant surface temperature in the DNS simulation. These results agree with the conclusions of Mukunda and Paul [11] showing that flow effects dominate the erosive burning contribution to the total burn rate. Although the surface temperature is assumed to remain fixed, the thermodynamic properties at the solid-gas interface are calibrated to produce the needed regression rate at the zero cross-flow condition, and are not expected to vary much as the regression rate increases. As will be shown, this is because  $(-E_A/R_u T_s)$  is very large, and thus produces large changes in the regression rate with small changes in the surface temperature [14].

Figure 15 shows the change in the thermal boundary layer as the Mach Number increases.

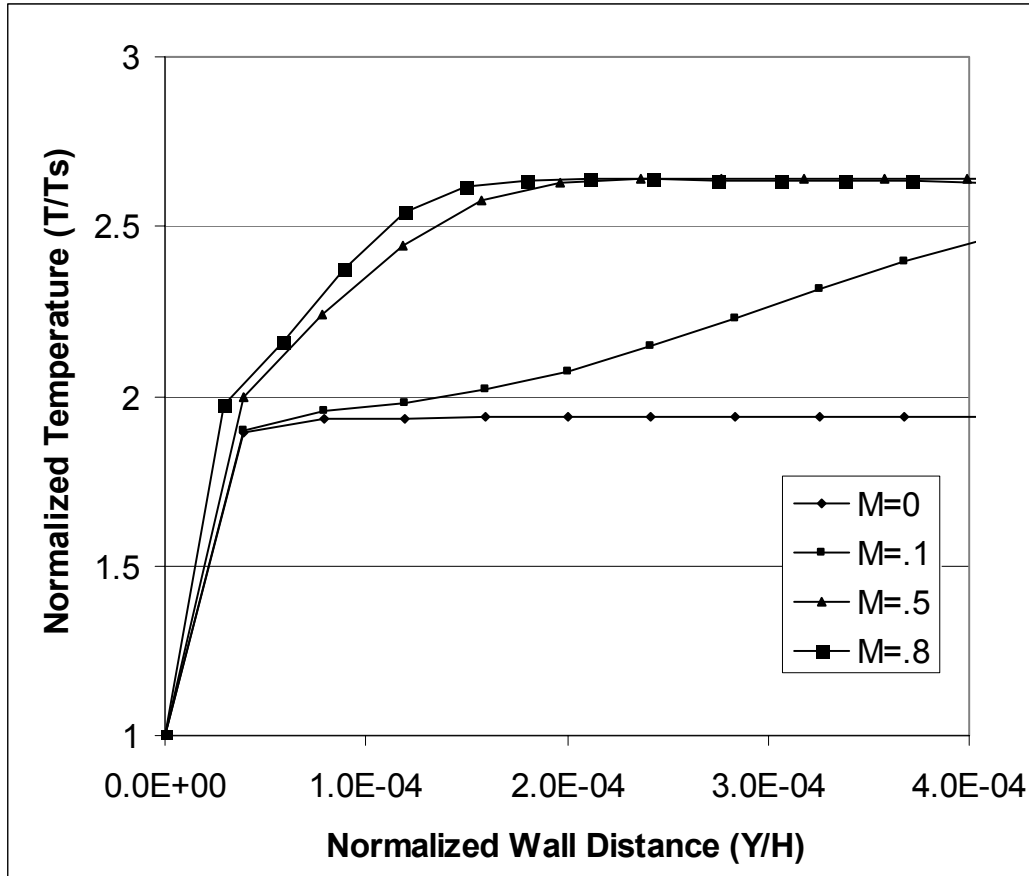
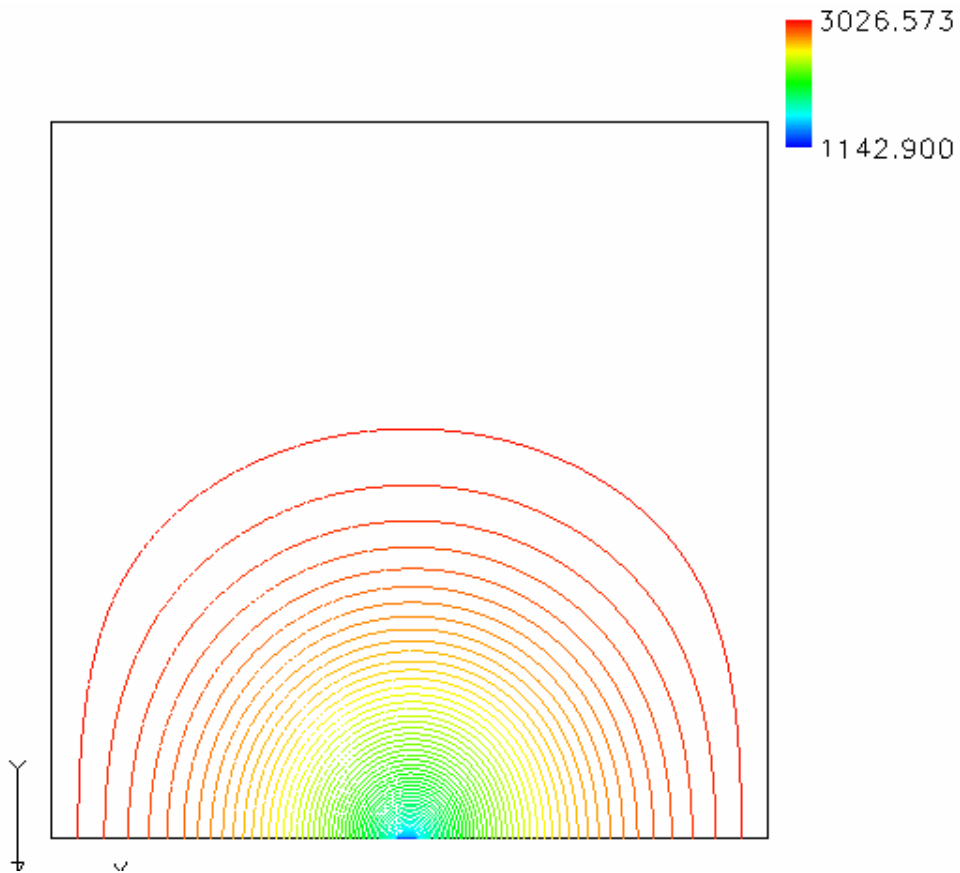


**Figure 15 Thermal Boundary Layer Profiles**

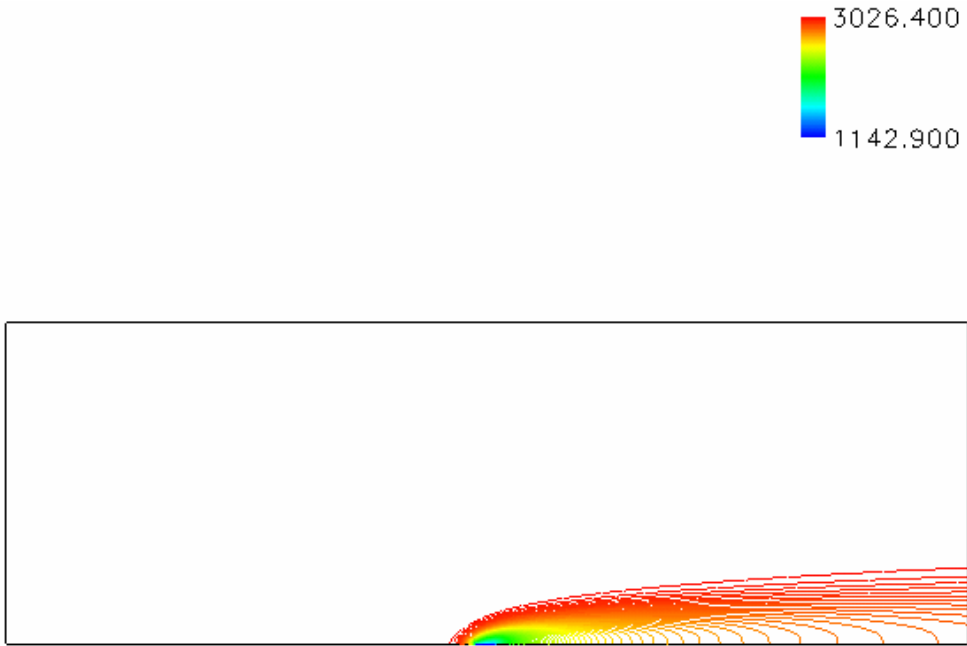
The plots show a large temperature jump between the wall and the first grid cell. This jump is due to the infinite rate chemistry model in conjunction with an estimate of the surface temperature, where the calibration is achieved by varying the heat of pyrolysis. To account for this jump, the gas side temperature gradient is calculated with a high order scheme.

As the Mach Number is increased, the thickness of the thermal boundary is reduced, increasing the heat transfer to the surface, and thus the regression rate. This is illustrated in Figures 16, 17, and 18, where temperature contours are plotted for three

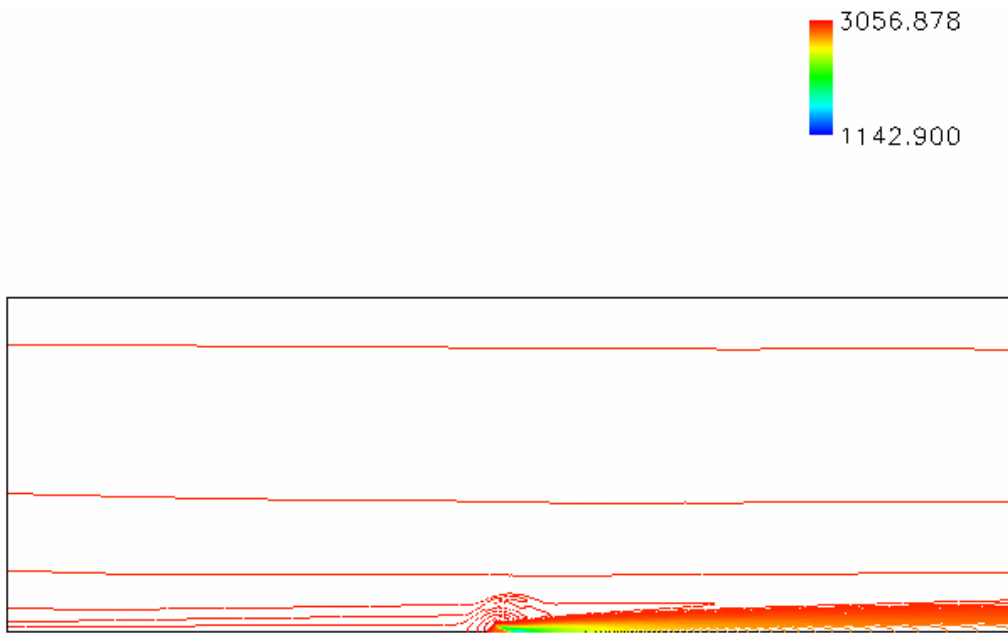
free-stream Mach Numbers. These contours are not of the complete computational domain, but are taken in the vicinity of the propellant.



**Figure 16 Temperature (K) Contours ( $M=0$ .)**

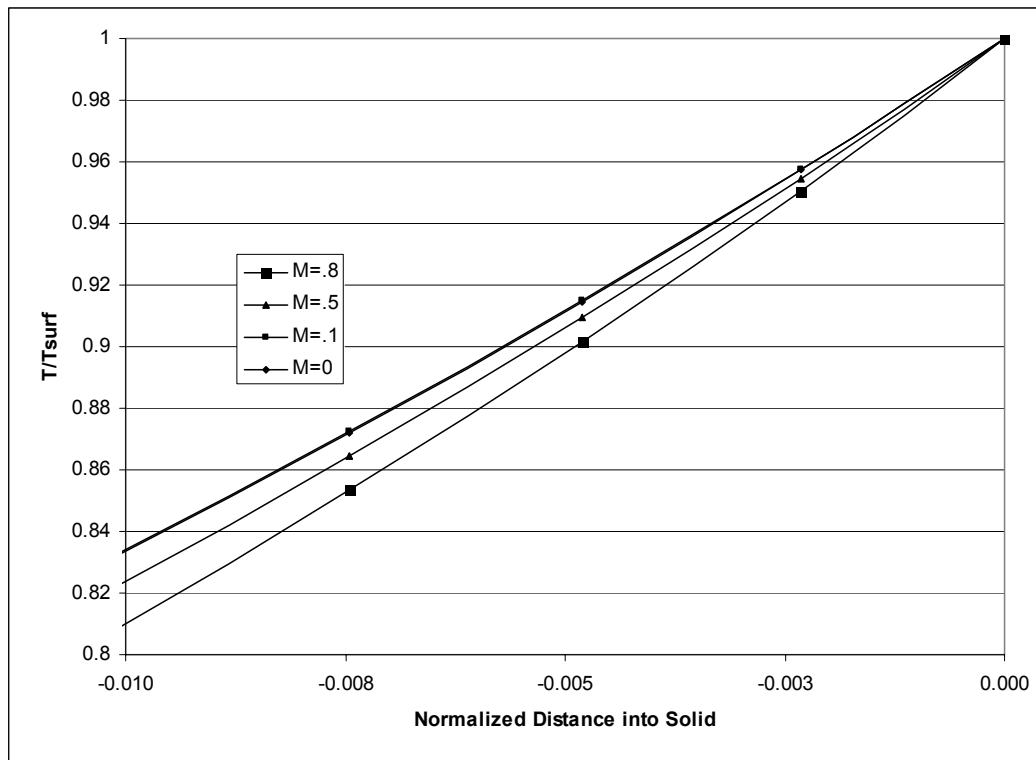


**Figure 17 Temperature (K) Contours ( $M=.1$ )**



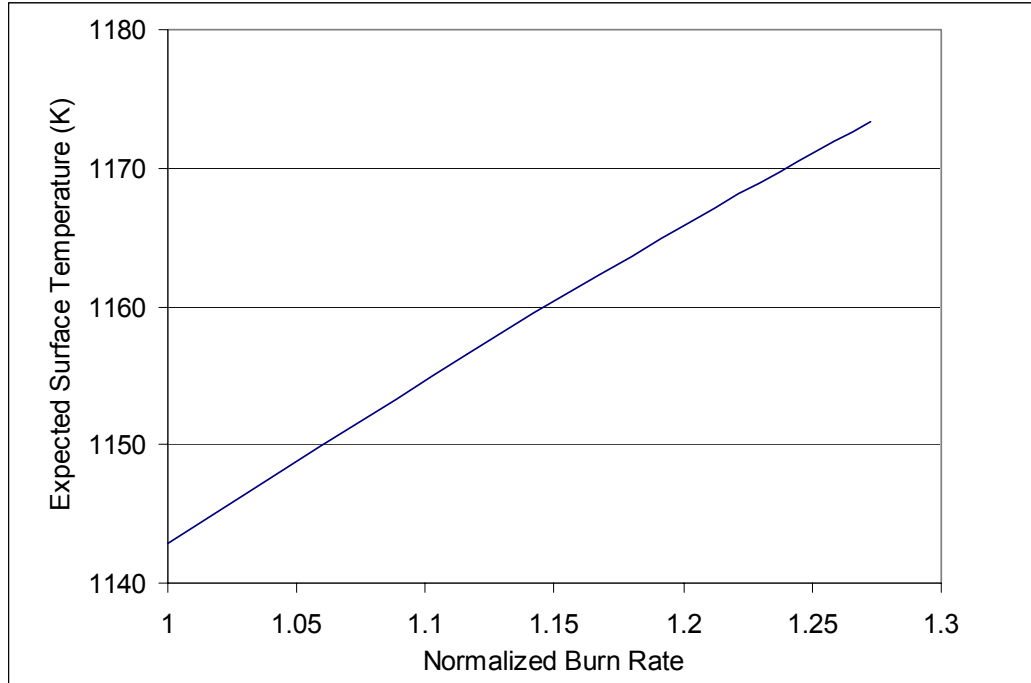
**Figure 18 Temperature (K) Contours ( $M=.5$ )**

Figure 19 shows the thermal gradient in the solid at the time of convergence. As the heating rate on the surface increases, the gradient in the solid becomes steeper, as expected.



**Figure 19 Temperature Profile in the Solid**

Using Equation 7, the expected surface temperature versus regression rate is plotted in Figure 20, where the assumed surface temperature of  $1143.0\text{ K}$  is used as  $T_{surf_o}$ .



**Figure 20 Expected Surface Temperature versus Normalized Burn Rate**

The figure shows that with an *18%* increase in burning rate, the surface temperature is expected to increase only approximately *1.8%*. This very modest increase in temperature should have minimal effect on the general flow field, thermal transport properties at the surface, and the slope of the thermal gradient at the surface.

#### *5.4 Varying Surface Temperature Analysis*

To examine the impact of assuming a constant surface temperature in the previous analysis, a single DNS calculation is conducted for a free stream Mach Number of  $M=0.1$ . The surface temperature is calculated via a surface energy balance, in conjunction with Equation 7, where  $T_{Ref-s}$  is assumed to be *1143.03 K*. The calculations are run on the same grid as the fixed surface temperature analysis, and are carried out until a steady time average regression rate is achieved. The results of the analysis show that the converged

surface temperature rises to  $1145.6\text{ K}$ , for a  $0.22\%$  increase over the reference condition. The converged normalized burn rate is calculated to be  $1.0179$  compared to the fixed temperature case at  $M=0.1$  of  $1.015$ . These results show that the fixed surface temperature assumption results in a modest  $0.29\%$  difference in the predicted solution as compared to the floating surface temperature calculations.

Figure 21 shows a comparison of the thermal boundary layers of the fixed and floating surface temperature cases for  $M=0.1$  normalized by the reference surface temperature of  $1143.0\text{ K}$ . The curves show very little difference, as would be expected with the minimal change in temperature.

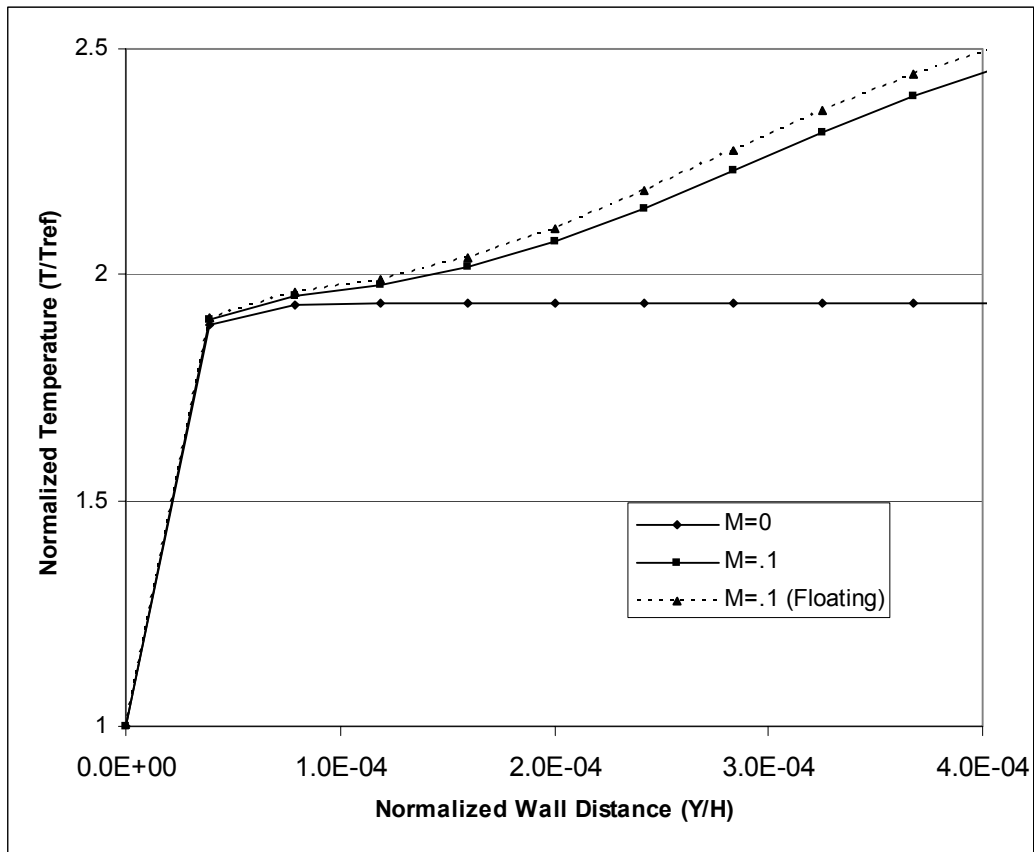


**Figure 21 Comparison of Thermal Boundary Layer**

### *5.5 Universalism of the Infinite Rate Chemistry Model*

For a DNS generated erosive burning model to be useful to the design engineer, the assumptions and methodology used to produce the models must be shown to be universal in nature, and not geometry specific. Development of an erosive burning model through DNS for a given propellant is time consuming, and would not be very advantageous to the designer if the model is extremely motor geometry specific such that it must be regenerated after each geometry design change. Typically, in a motor design process, the propellant will be selected or developed, and then will experience few significant formulation changes thereafter. If the DNS model can be shown to be weakly dependent on the full scale motor geometry, then the designer can universally apply the DNS model to different configurations, assuming the propellant formulation remains relatively constant.

In Section 5.3.3 the infinite rate DNS model is used to calculate the performance of the CKEM-4 rocket motor. Test data for several other CKEM configurations exist that contain the same propellant as the CKEM-4, but of slightly different propellant geometry, and/or throat erosion histories. The net result of these differences is a modification to the average internal pressure, Mach Numbers, flow field, and induced erosive burning.

The DNS model used to predict the performance of the CKEM-4 motor, is again used to predict the performance of the CKEM-9 motor. The model is implemented in the ballistics code in the same way as in the previous analysis. Figure 22 shows a comparison of the predicted results of CKEM-9 to the static test data. Also shown in the figure is the CKEM-4 static test data.

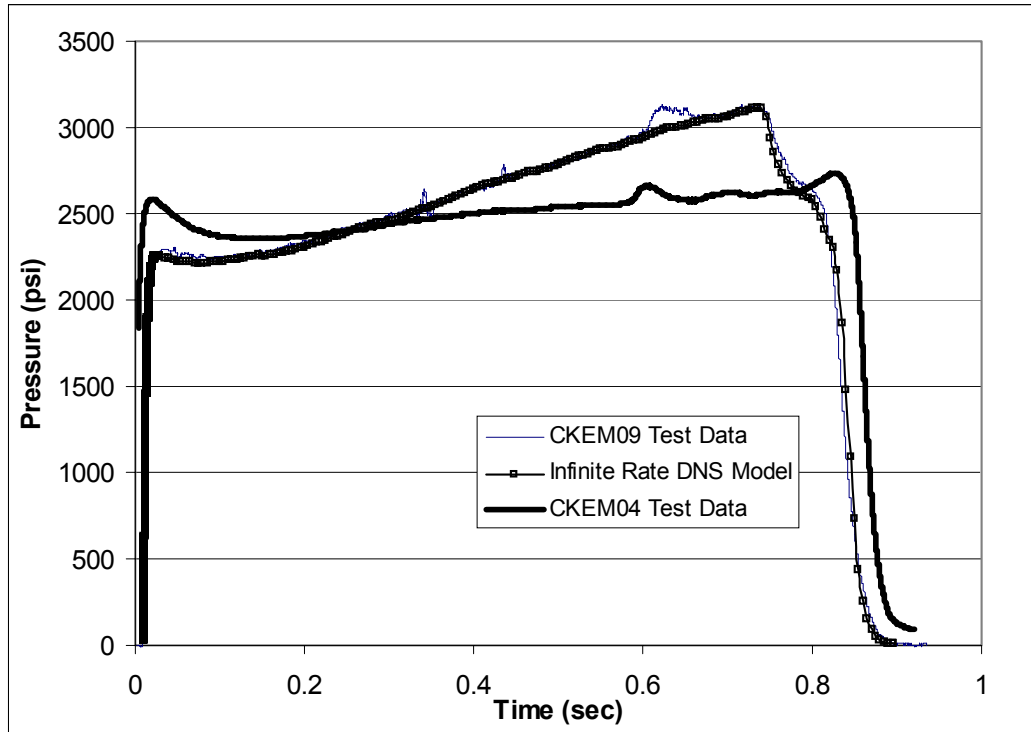


**Figure 22 Ballistics Analysis of CKEM-9 Using DNS Model**

A comparison of the test data between CKEM-4 and CKEM-9 show a noticeable difference in the pressure peaks that occur shortly after ignition. Typically, the magnitude of these pressure peaks are indicative of the amount of erosive burning present in a motor (Other causes for initial pressure peaks may include a nozzle closure, robust igniter, etc.). In addition, the average operating pressures of the two designs are different, but not substantially. Thus, these two designs represent different test conditions for the DNS model. As the figure shows, the model has performed as well in the second case as in the first, indicating that the DNS model is not strongly dependent on the full scale geometry. These results are reasonable since the only connection between the DNS calculations, and the full scale geometry is in establishing the integral scales for the turbulent velocity profile boundary condition at the entrance.

### *5.6 Thermal Boundary Layer Profile Dependency*

The primary mechanism effecting erosive burning is increased heat transfer from the free-stream, through the boundary layer, down to the propellant surface. The rate of heat flow through the boundary layer is dependent on the thermal profile, and thus dependent on the thermal boundary condition at the entrance of the computational domain. A fully developed turbulent velocity profile is prescribed at the entrance of the domain for all analyses. The thermal profile is set by assuming constant stagnation temperature across the entrance plane with the static temperature set according to isentropic flow relations. Thus, the entrance velocity profile corresponds to an adiabatic wall profile.

From the entrance to the burning propellant, the wall boundary condition is set as adiabatic, thus, the thermal boundary layer profile does not develop between the entrance and the burning propellant. The width of the burning propellant in the infinite rate model is set at approximately 2% of the total width of the computation domain, and is placed in the center. The purpose of this is to remove the combustion process away from the influence of the boundary conditions at the entrance and exit. With these boundary conditions, the only portion of the bottom wall of the computational domain where the wall boundary condition is not adiabatic is over the burning propellant.

In a full scale rocket motor, heat transfer at the bounding wall (burning propellant surface) will begin at the head-end of the motor, and continue to the aft. Thus, the thermal boundary layer will be continuously influenced by the heat transfer condition at the wall. To examine the influence of the thermal boundary layer growth on the predicted erosive burning, an additional DNS calculation is made at a free-stream Mach

Number of  $M=0.1$ , where the width of the propellant is increased to 50% of the width of the domain. All other boundary conditions are identical to those stated for the original calculation at the same Mach Number.

Plotted in the figures below are surface values for the 50% width and the 2% width analyses. In each of the plots, the local value is normalized by the value at the mid-point of the burning propellant. The length scale in each plot is normalized by the 50% width length.

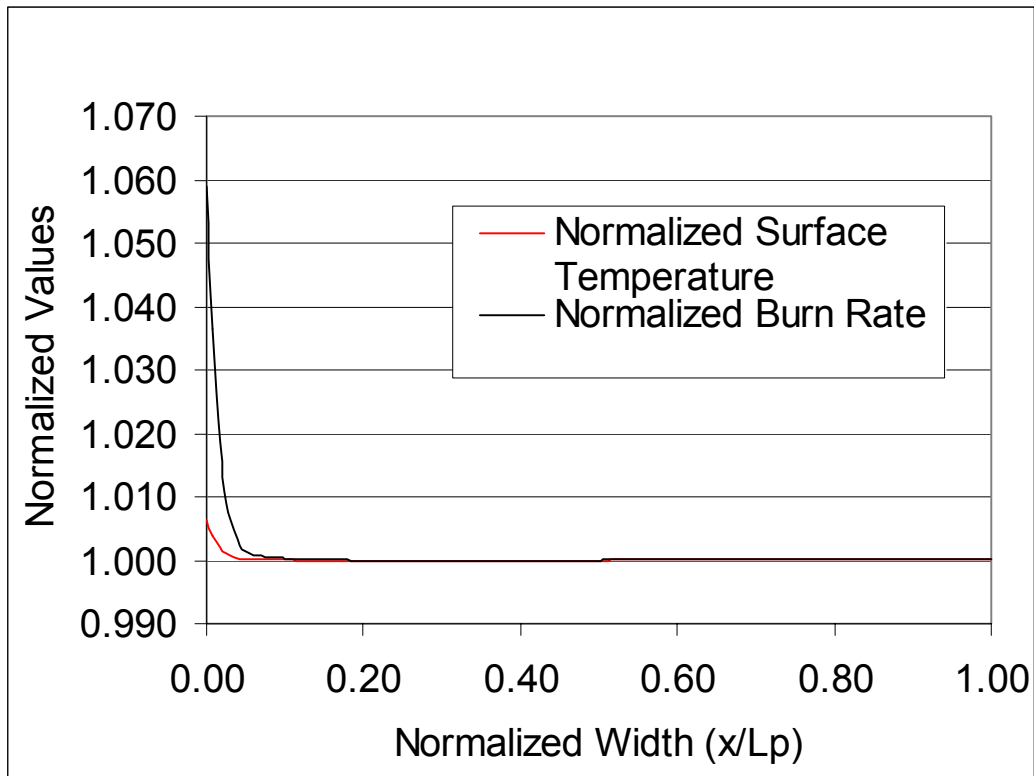


**Figure 23 Normalized Surface Values for the 50% Width Case**

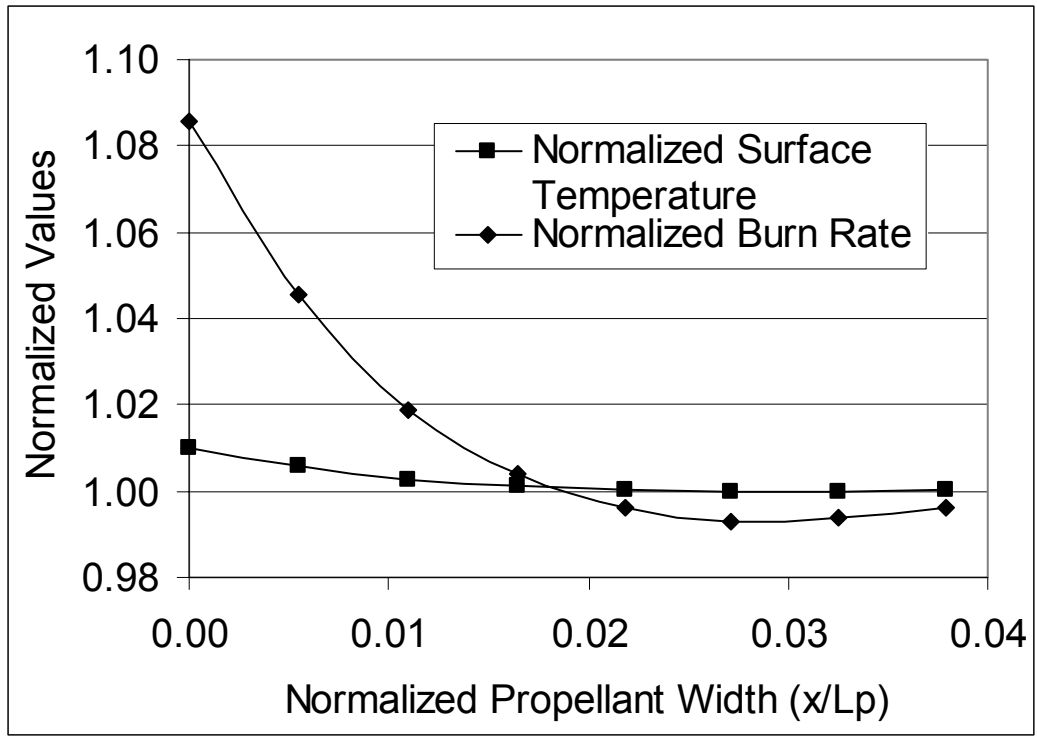


Figure 24 Normalized Surface Values for the 2% Width Case

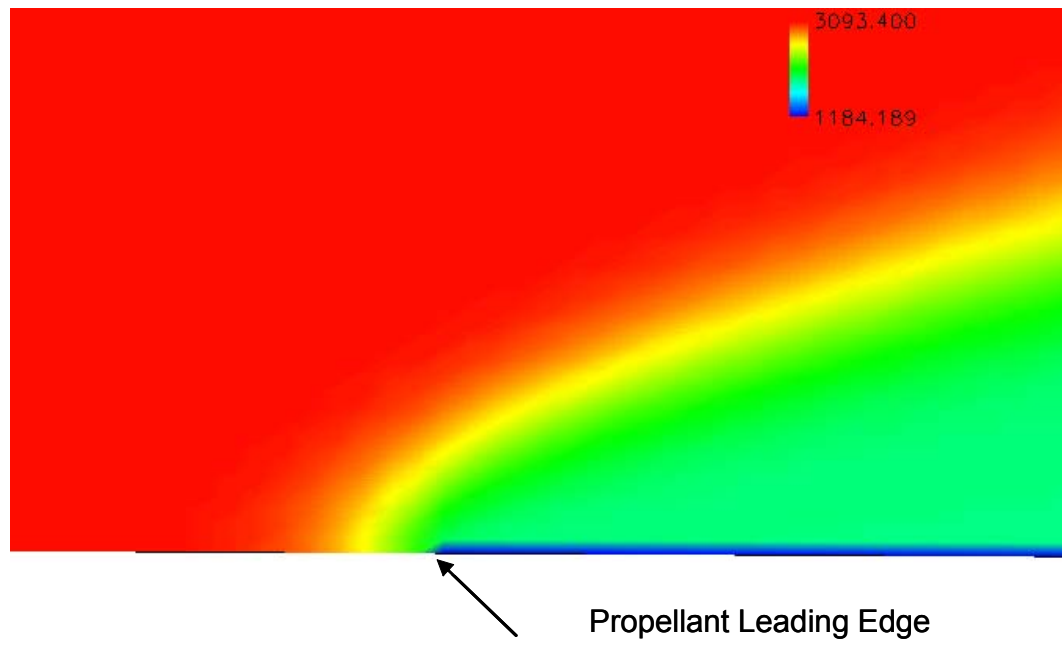
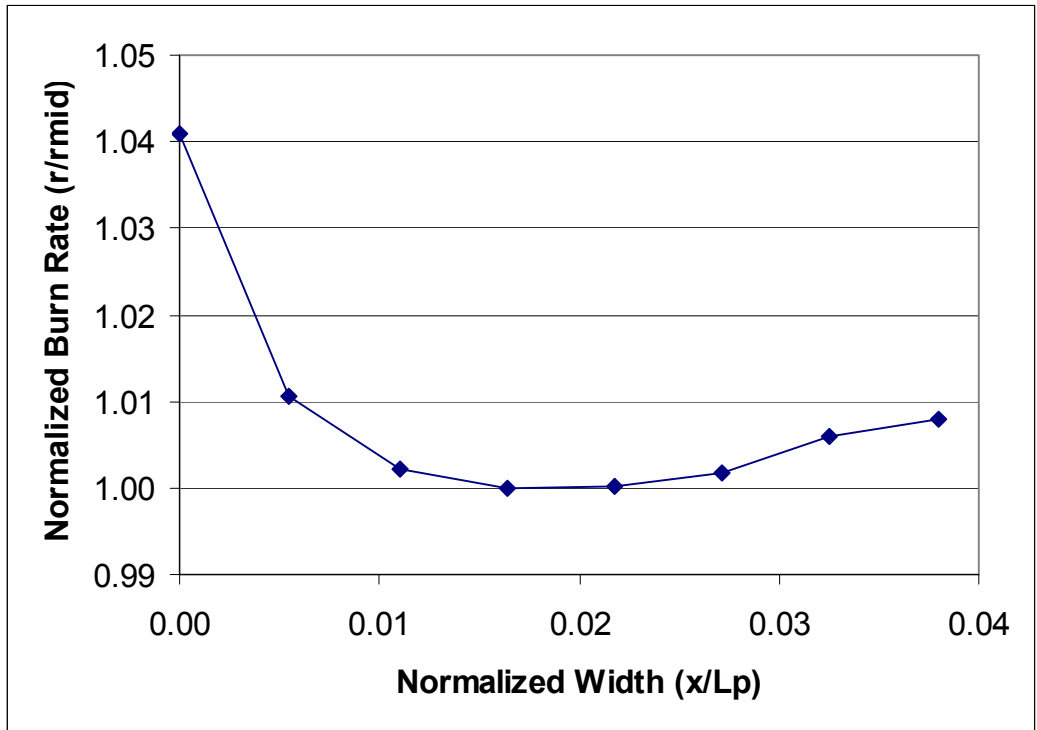


Figure 25 Thermal Contours at the Leading Edge of the Propellant (K)

The figures show similar behavior between the two analyses. In both cases, the leading edge of the burning propellant has a sharp rise in the calculated burning rate. As Figure 25 shows, this is due to the high temperature gradient (heating rate from the free-stream) that exists at the leading edge. Beyond the leading edge effects, both analyses show a gradual rise in burn rate along the width of the propellant. This is attributed to the development of the thermal boundary layer above the burning surface. However, as Figure 23 shows, for the wider propellant strip, this increase is very small. The most significant conclusion from this analysis is that the wider propellant reduces the influence of the leading edge effect over the surface of the propellant, and allows for a more representative calculation of the burning rate. Shown below in Figure 26 is the normalized burn rate profile for an  $M=0.1$  free-stream where the surface temperature is held constant, as in the infinite rate erosive burning model analyses. Although the propellant width in this analysis is 2%, the leading edge effect is much less pronounced than in the floating temperature analysis.



**Figure 26 Fixed Surface Temperature Burn Rate Profile**

Since surface average conditions are used to calibrate the erosive burning models to the strand data, calculating a standard deviation based on length for each of the three methods gives some indication of the better approach to modeling the burning surface. The standard deviation for the three normalized rates are  $\sigma = 0.0332$ ,  $0.0136$ , and  $0.0059$  for the short floating case, the short fixed case, and the long floating case, respectively. The source of this variability comes from the relative influence that the leading and trailing edge effects have on the interior calculation points on the burning surface. From these results, increasing the propellant width seems to be the best approach in reducing the dispersion of the calculated regression along the width of the propellant surface.

To complete this analysis, the 50% width case is re-run using the converged thermal profile at the exit of the computational domain as an entrance boundary condition.

The purpose of this analysis to see if the thermal boundary layer continues to develop, and if so, what influence this has on the calculated burn rate. Figure 27 shows an entrance temperature profile based on isentropic flow relationships. This profile is typical of the boundary conditions used in the erosive burning calculations.

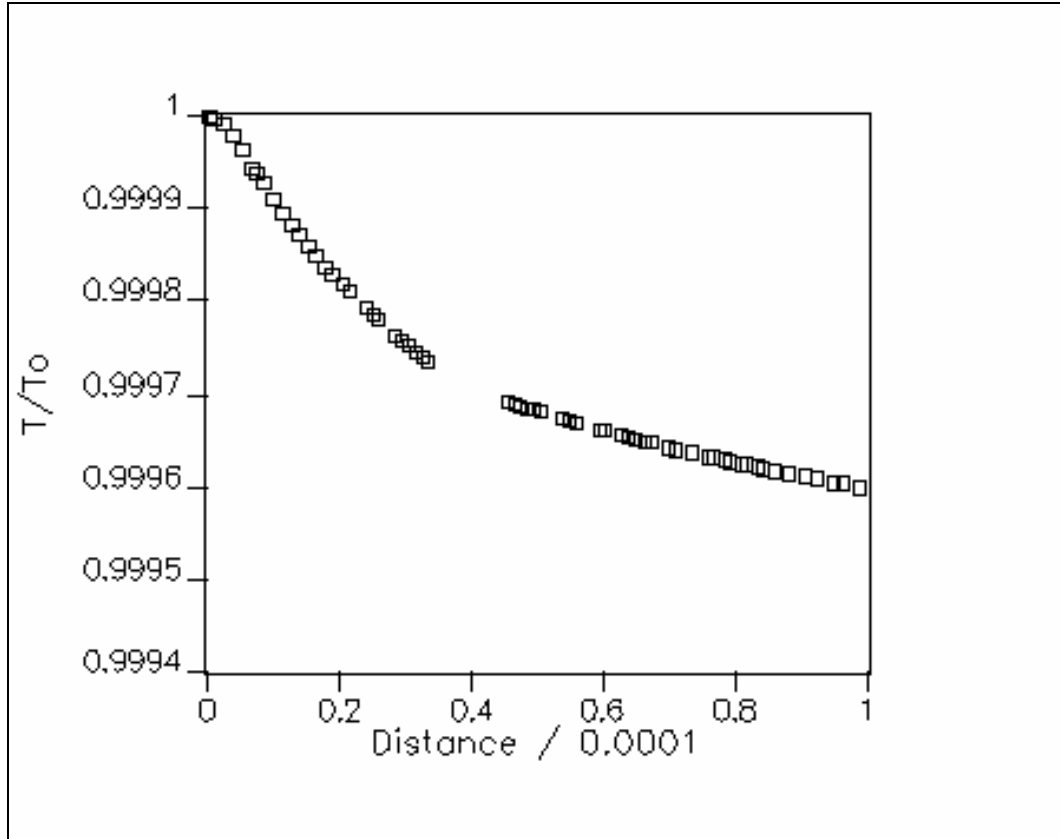


**Figure 27 Entrance Temperature Profile from Isentropic Flow Relationships**

Figure 28 shows the temperature profile taken from the exit plane of the 50% propellant width analysis, which is used as the input condition for the present analysis. The profile shows the effects of heat transfer into the propellant solid.

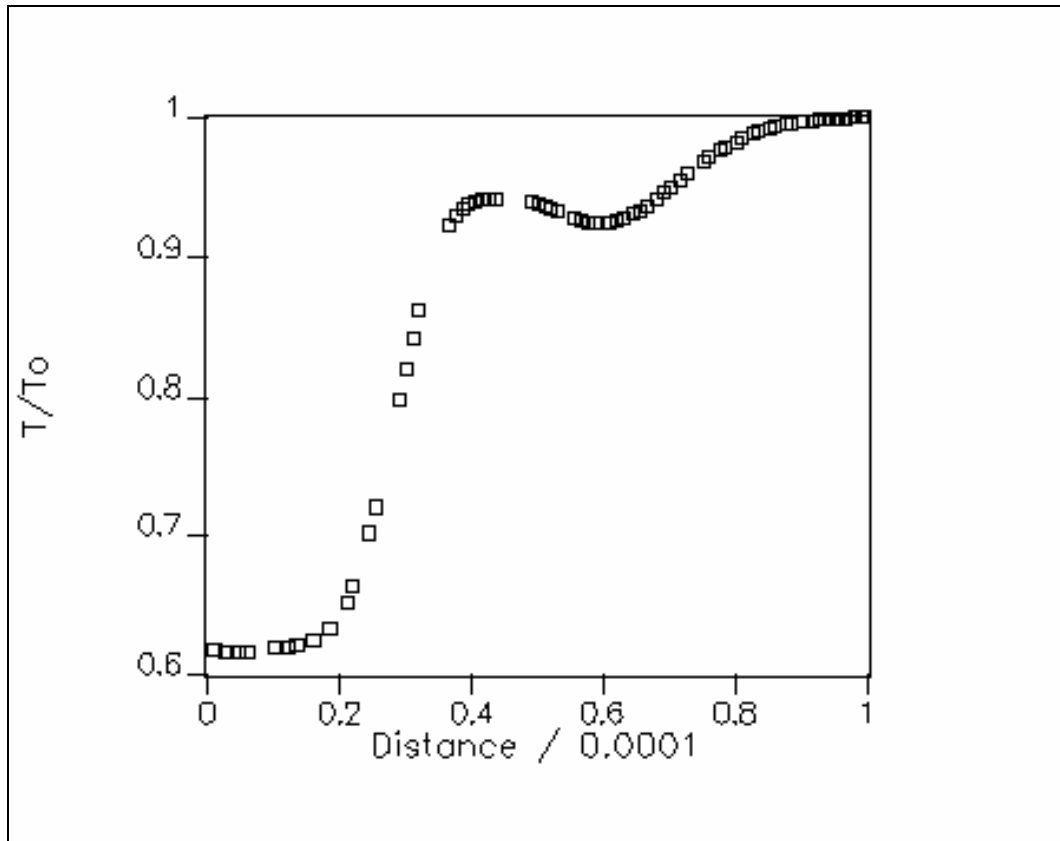


**Figure 28 Entrance Temperature Profile with Wall Heat Transfer**

Figure 29 shows a plot of the results of the analysis plotted with the results of the previous 50% propellant width analysis. The temperatures in the plot are normalized by the mid-width surface temperature of the isentropic flow entrance case. One noticeable characteristic missing from the developed thermal profile analysis is the sharp temperature rise at the leading edge. This is expected since the fluid at the leading edge is now at a lower temperature than in the isentropic entrance. Of most significance is that the surface temperature of the modified entrance analysis and the isentropic analysis approach the same value shortly behind the leading edge. This leads to the conclusion that the thermal boundary layer develops very rapidly above the burning surface. The

wider propellant strip allows for the leading edge effect to diminish with length such that the regression rate approaches a near constant value along the surface.

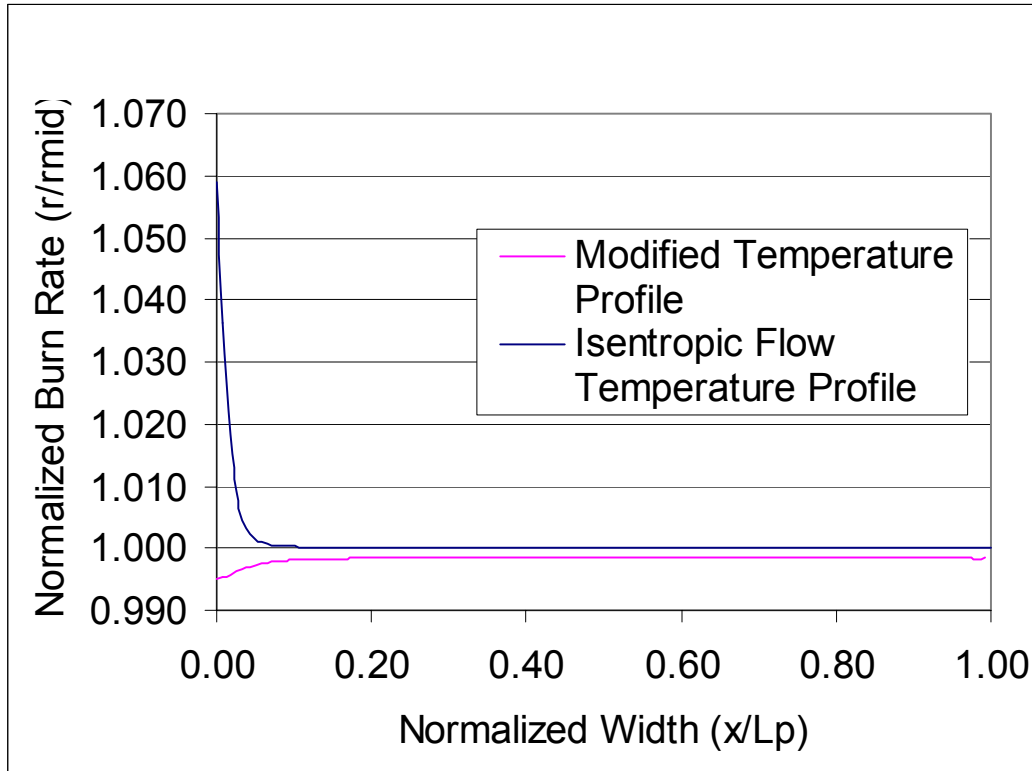


**Figure 29 Burn Rate Comparison for Isentropic and Modified Entrance Temperature Profiles**

### 5.7.0 Finite Rate Chemistry Model Overview

The primary mechanism in erosive burning is the augmentation of transport properties in the boundary layer due to turbulent mixing. The infinite rate chemistry model provides a convenient means of isolating and studying this mechanism. The results of the infinite rate DNS model agrees with the literature and produces an erosive burning model that gives excellent results in the ballistics analysis of full scale motors.

The secondary contributors to erosive burning are related to the combustion process, and must be studied using finite rate chemistry.

In the flame zone above the solid propellant, several heat release regions exist at varying distances from the propellant surface. The most influential of these flames are the premixed exothermic decomposition of AP, and the flame of decomposed AP and binder gases. The heat feedback from these flames and from the free stream to the propellant surface determines the rate at which the propellant will pyrolyze.

The reaction rate of the AP decomposition is very fast [17], compared to the binder to APd reaction. Since the decomposition flame is premixed, turbulent augmentation diffusion is irrelevant. The location of the flame will be determined from a balance between the unreacted gas mixture's species velocity originating from the propellant surface, and the reaction rate of the decomposition process. Consequentially, the location of the APd flame is not expected to be influenced substantially by the addition of cross-flow. However, since the reaction rate is temperature dependent, a change in the temperature profile through the boundary layer as a result of cross-flow will impact the reaction rate profile of the APd and heat feedback from the flame.

The flame between the APd and the HTPB binder is influenced by the turbulent boundary layer in cross-flow. As the cross-flow increases, and the turbulent intensity increases, the diffusion time of the two species will be decreased. As such, the standoff distance of the flame, and thus the flame thickness, should decrease. In addition, a compression of the thermal boundary layer will impact the reaction rate, as in the APd flame.

The purpose of this study is to investigate the magnitude of the influence cross-flow has on the above described mechanisms. Based on other studies [11], the chemistry time scales are expected to be much smaller than the flow time scales, and thus will show negligible correlation to the free stream cross flow velocity. The propellant in consideration contains small (37 micron), evenly distributed AP particles. The gases are assumed to flux of the surface of the burning propellant at a constant mass fraction; thus they are premixed. This assumption is assumed applicable for small AP only.

### 5.7.1 Model Definition and Boundary Conditions

The mass fractions of all species that are considered are set at the boundaries, as well as initially throughout the computational domain. Heats of formation for all species are specified such that the split of chemical energy to sensible energy may be tracked. In addition, species diffusion velocities are calculated, and thus require the input of mass diffusivities. Finally, reaction rates are specified for all chemical reactions considered.

The total heat release from all reactions is set equal to the adiabatic heat release of the propellant as calculated by thermochemical equilibrium. Since only two reactions are considered, the heat release from the APd flame and the APd-HTPB flame must be equal to the total heat release from the propellant. For an adiabatic system, the total enthalpy of a reaction is constant; only the distribution between sensible and chemical enthalpy changes as shown below.

$$\begin{aligned} (h_f^o + h_s)_{AP} &= (h_f^o + h_s)_{APd} \\ \eta(h_f^o + h_s)_{APd} + (1-\eta)(h_f^o + h_s)_{HTPB} &= (h_f^o + h_s)_{Products} \end{aligned} \quad (28)$$

In the above equations,  $\eta$  represents the mass fraction of the APd in the APd-HTPB reaction. Two thermochemical equilibrium calculations are run. The first calculation is

to find the adiabatic heat release, or sensible enthalpy of the APd reaction. Knowing this, along with the heat of formation of the AP, the heat of formation of the APd is calculated. The heat of formation of the final combustion products is then found from Equation 28 by setting  $h_s$  of the products to the thermochemical calculation value, and  $h_s$  of the HTPB to the tabulated value. Table 2 shows the results.

**Table 2 Heats of Formation of Considered Species**

Ammonium Perchlorate - $h_f^o$	-2520.51 kJ/kg
Ammonium Perchlorate - $h_s$	0.0 (at Ref. Condition of 298. K)
Ammonium Perchlorate Decomposed - $h_f^o$	-4092.68 kJ/kg
Ammonium Perchlorate Decomposed - $h_s$	1572.17 kJ/kg
HTPB - $h_f^o$	-1001.5 kJ/kg
HTPB - $h_s$	0.0 (at Ref. Condition of 298. K)
Combustion Products - $h_f^o$	-7213.19 kJ/kg
Combustion Products - $h_s$	5032.4 kJ/kg
$\eta$	0.8901

All species are also considered to have the same mass diffusivities, found from the Lewis Number ( $Le = \alpha/D$ , where  $\alpha$  is the thermal diffusivity, and  $D$  is the mass diffusivity).

**Table 3 Finite Rate Model Gas Properties**

<i>MW</i>	<i>27.3 kg/kmol</i>
<i>C<sub>p</sub></i>	<i>1800.2 J/kg</i>
<i>Pr</i>	<i>0.6</i>
<i>Le</i>	<i>1.0</i>

### 5.7.2 Chemical Mechanism

The four chemical species considered in the analysis are AP gas, APd gas, binder gas, and combustion products. Two chemical equations, shown in Equation 29, are required to relate these species in the chemical model.



In the above equation,  $\beta$  is the mass stoichiometric coefficient. Two global reaction rate equations [17] are required to complete the chemical model and are shown in Equation 30

$$\begin{aligned}
 R_1 &= D_1 P_o^{n_1} [AP] \exp\left\{-\frac{E_1}{R_u T}\right\} \\
 R_2 &= D_2 P_o^{n_2} [APd][Binder_{Gas}] \exp\left\{-\frac{E_2}{R_u T}\right\}
 \end{aligned}
 \tag{30}$$

-where the  $[ ]$  quantities are the concentrations of the species, and  $D_i$ ,  $n_i$ , and  $E_i$  have been taken from previous studies [14] [17] and represent experimental data. The law of mass action is used to complete the rate of production of the remaining two species. Table 4 summarizes the data used in the chemistry model.

**Table 4 Finite Rate Chemistry Model Input**

$D_1$	$2.234 \times 10^7$
$D_2$	$1.105 \times 10^7$
$E_1/R_u$	8000 K
$E_2/R_u$	11000 K
$n_1, n_2$	1.0
$\beta$	8.1

### 5.7.3 Model Calibration Procedure

The initial step in developing the finite rate chemistry model is to calibrate the analysis to strand burner data. In the calibration step, no cross-flow is induced, with boundary conditions set such that the domain pressure will converge to the desired value at infinity. Equation (21) is used to describe the pyrolysis rate as a function of temperature and pressure. A reference burn rate and reference temperature of  $0.17 \text{ cm/s}$  and  $835 \text{ K}$  respectively are chosen from the literature [14], for a similarly formulated propellant. The solution is allowed to converge to the regression rate and surface temperature that produces an energy balance at the surface. This regression rate is compared to strand burn rate data. If the calculated regression rate and the measured regression rate do not match, the heat of pyrolysis (other variables can be used, surface temperature, gas and solid conductivity, etc.) is adjusted, and the procedure repeated. Once the model is calibrated to the strand burn rate data through the adjustment of the heat of pyrolysis, cross-flow is induced, holding the calibrated properties constant.

The selection of the reference temperature and reference rate is not viewed as highly critical in this analysis, but serves as a reasonable starting point for the calibration step. Minor ingredients can produce drastic changes in the regression rate of a propellant. The calibration step is critical to establish the proper base burning rate for the particular propellant in the analysis at the no cross-flow condition. Several other variables exist in the model which are candidates for use in the calibration step. Since the regression rate is ultimately determined by the energy balance at the solid-gas interface, the most likely candidates are the solid conductivity, the gas conductivity, and the heat of pyrolysis. The solid conductivity is not significantly altered by minor ingredients, is easily measured, and can be selected from data of any propellant with similar mass ratios of AP and HTPB. Both the gas conductivity and the heat of pyrolysis can be greatly effected by minor ingredients, and have more uncertainty in their true values. Since altering the gas conductivity will either change the Prandtl Number, or also change the gas viscosity (holding the Pr constant), the heat of pyrolysis is chosen as the calibration variable. The calibration steps in the analysis produce heats of pyrolysis that are very reasonable, and are in the range of values published for an AP/HTPB propellant.

#### *5.7.4 Finite Rate Model Results*

The results of the finite rate analysis are shown in Table 5, showing also the calculated rates normalized by the  $M=0.0$  values. The calibration run for  $M=0.0$  results in a surface temperature of  $1143.8\text{ K}$ . The normalized rate increase ranges from  $2.8\%$  at  $M=0.1$ , up to  $22\%$  at a free stream Mach Number of  $M=0.8$ . The normalized surface temperature increases associated with the predicted rates range from  $0.28\%$  at  $M=0.1$  up

to 2.0% at  $M=0.8$ . The results show that the surface temperature increase is small compared to the rate increase, due to the high activation energy in the pyrolysis law.

**Table 5 Finite Rate Model Results**

Mach Number	Rate (cm/s)	Surface Temperature (K)	Rate Ratio ( $r/r_0$ )
0.0	5.295	1143.8	1.0
0.1	5.444	1147.02	1.0028
0.5	6.018	1158.89	1.0132
0.8	6.453	1167.22	1.0205

Figure 30 shows a comparison of the near-wall temperature gradients in the normal direction at the mid-point of the burning propellant. The gradients are as expected, showing an increase in the gradient near the wall as the free-stream Mach Number increases. Figure 31 shows these gradients out to the extent of the thermal boundary layers. The increase in heat transfer to the wall as the Mach Number increases is evident in the curves. The curve for  $M=0.8$  shows considerable deviation from the isentropic and adiabatic entrance profile.

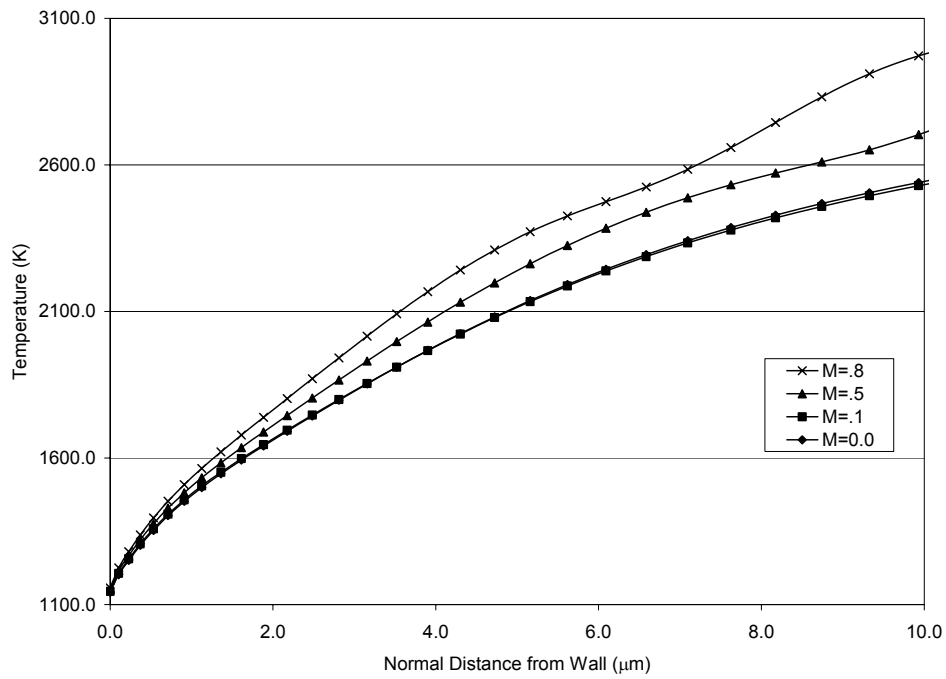


**Figure 30 Near Wall Temperature Profile**

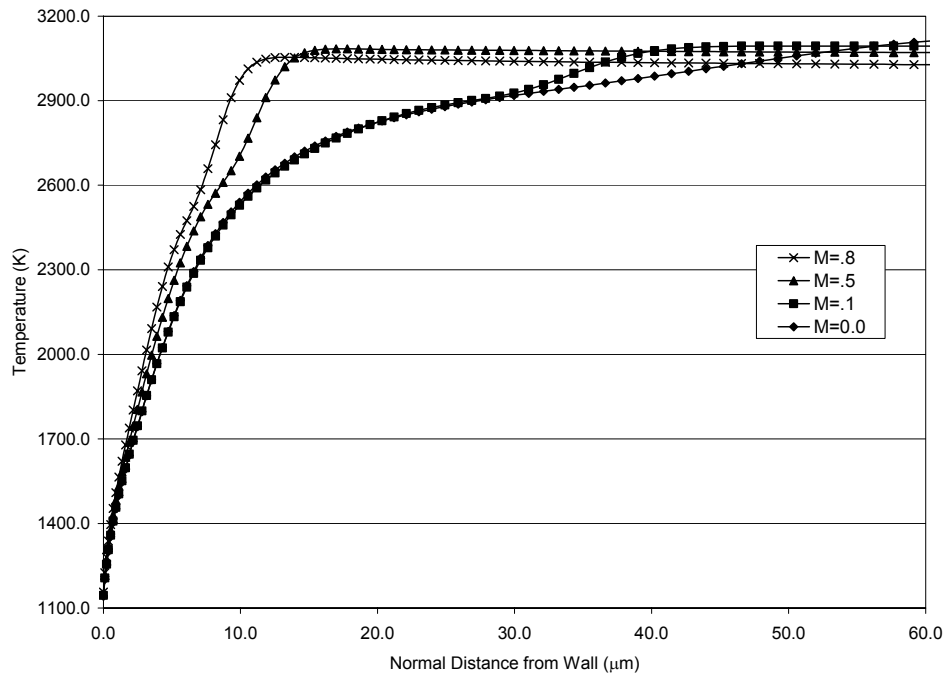


**Figure 31 Temperature Profiles out to Thermal Boundary Layer Edge**

The flame thicknesses for the AP decomposition flame and the APd-Binder flame are shown in Figure 32 for the  $M=0.0$  calibration analysis. The figure shows a very thin decomposition flame, which approaches the resolution limits of the model. However, several grid points exist between the wall, and the maximum reaction rate region. The flame is on the order of 3 microns thick. The premixed APd-binder flame is highly resolved, and approaches 40 microns in thickness.

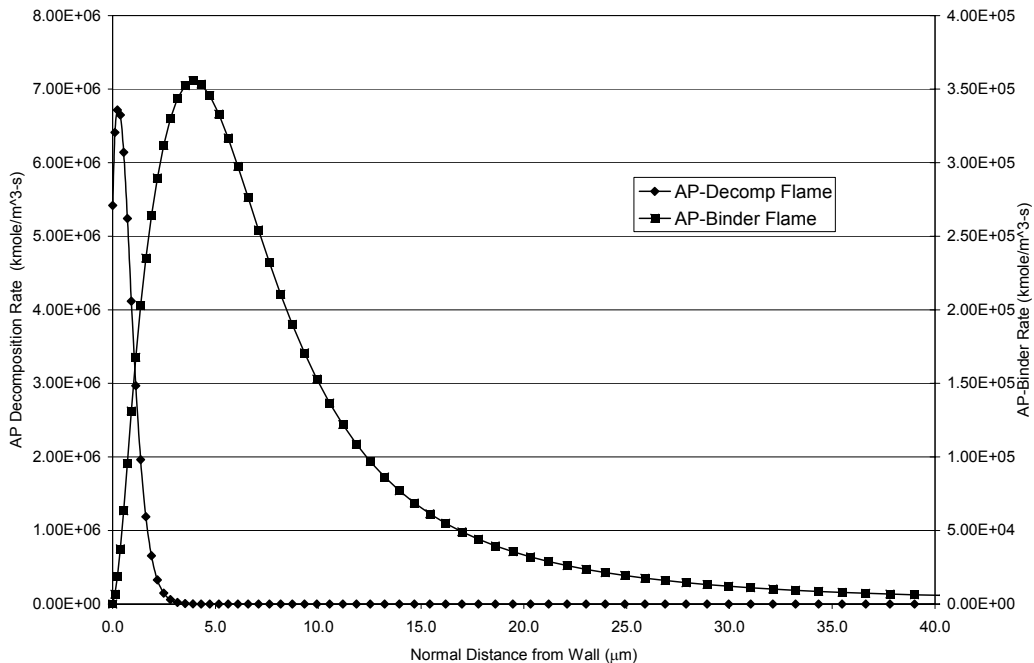


**Figure 32 Comparison of the AP Decomposition and APd-Binder Flame Thicknesses for  $M=0.0$**

Figures 33, and 34 show the effect of increasing the cross-flow velocity on the flame thicknesses. Of great interest is that as the Mach Number increases, the flame thicknesses decrease, but the relative distance of the maximum reaction rate from the wall

changes very little. Of note in Figure 34 is that the increase in Mach Number has very little effect on the AP decomposition flame thickness.

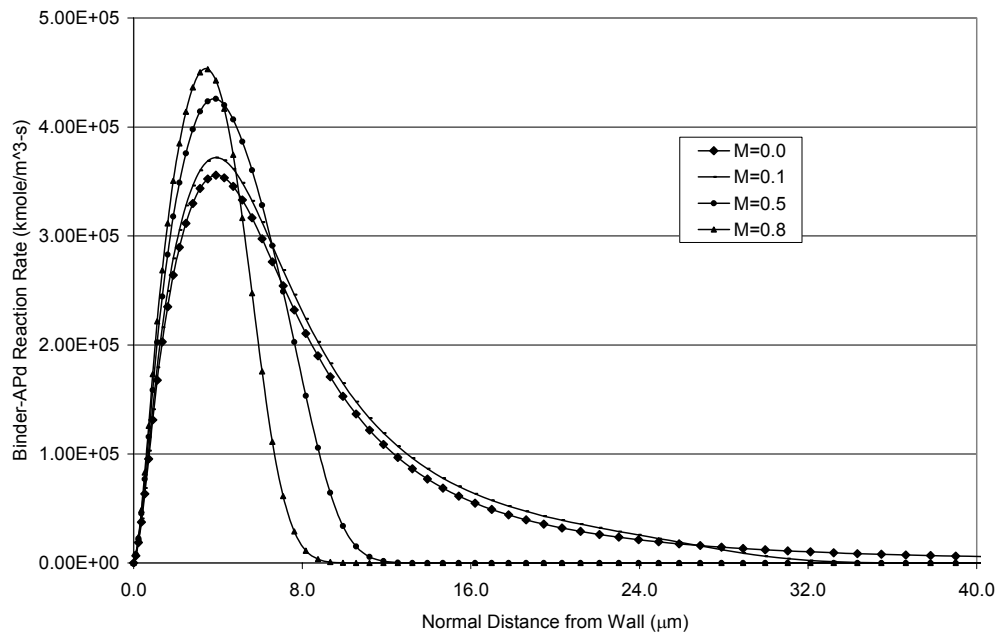


**Figure 33 APd-Binder Flame Thickness Comparison for Various Free-Stream Mach Numbers**

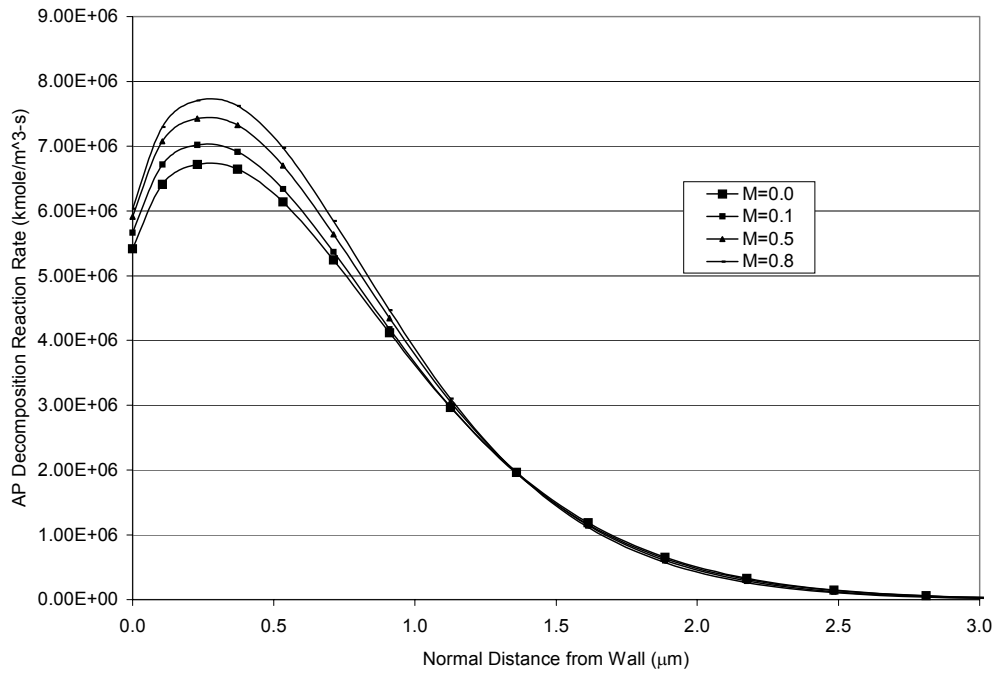


**Figure 34 AP Decomposition Flame Thickness Comparison for Various Free-Stream Mach Numbers**

Figure 35 shows that as the Mach Number increases, the near wall vorticity increases, with the maximum point moving close to the outer edge of the APd-binder flame. This is shown more clearly in Figure 36, where the APd-Binder flame is plotted with the vorticity for a free-stream Mach Number of  $M=0.8$ . The source of the vorticity is shown in Figure 37 where the tangential velocity profiles are plotted. The plot shows considerable lifting of the velocity boundary layer due to the side injection of the combustion gases, thus creating large tangential velocity gradients in the normal direction. The net result appears to be an increase in the reaction rate of the APd-binder flame, which results in a decrease in the flame thickness. The stand-off distance of the point of maximum heat release of the decomposition flame changes little.

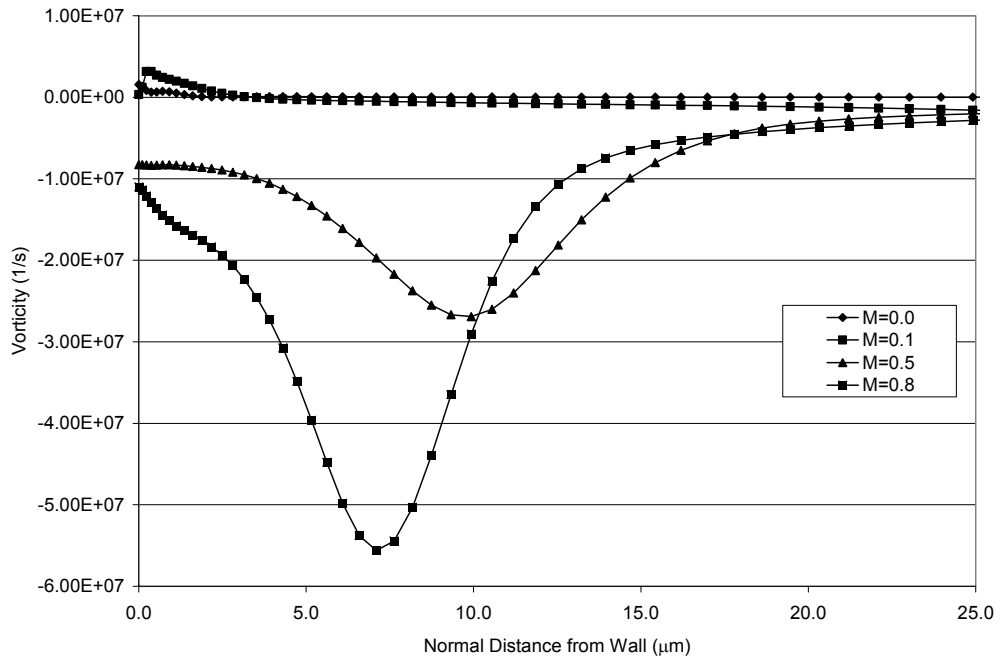


**Figure 35 Near-Wall Vorticity for Various Free-Stream Mach Numbers**

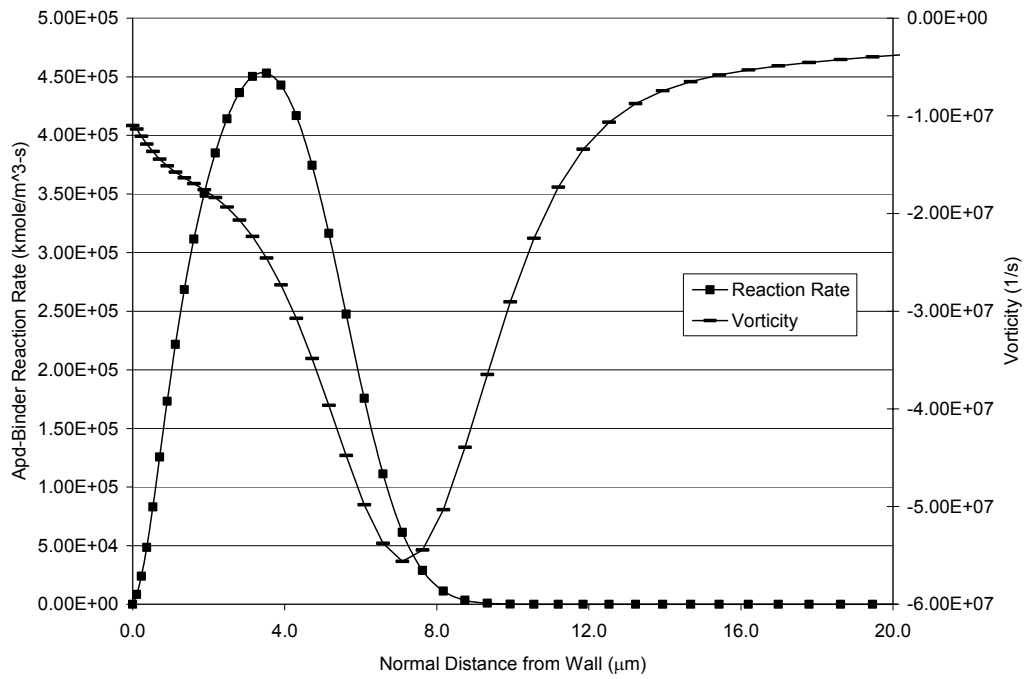


**Figure 36 APd-Binder Flame and Vorticity for  $M=0.8$**

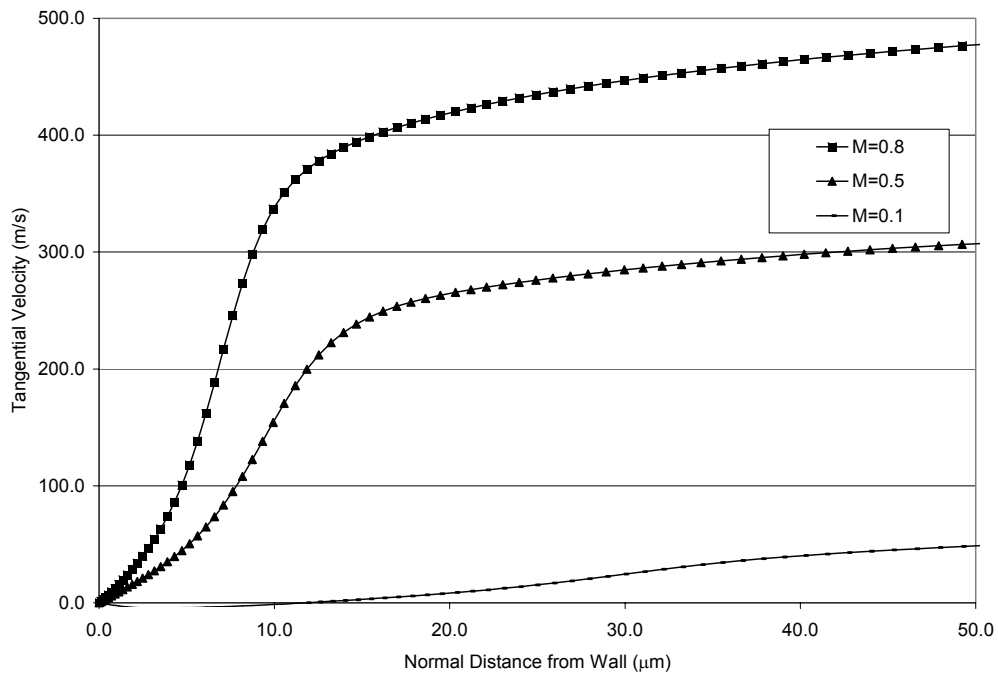


**Figure 37 Near Wall Tangential Velocity Profiles**

The starting location of the premixed APd-binder flame appears dependent on the pre-cursor AP decomposition flame. The results show that the decomposition flame thickness changes slightly with Mach Number, which is attributed to the temperature increase at the wall. Since there is little change in decomposition flame, the start of the APd-binder flame remains relatively stationary. Thus the results show that turbulent mixing reduces the APd-binder flame thickness, but does not significantly change the stand-off distance of the location of the maximum heat release zone.

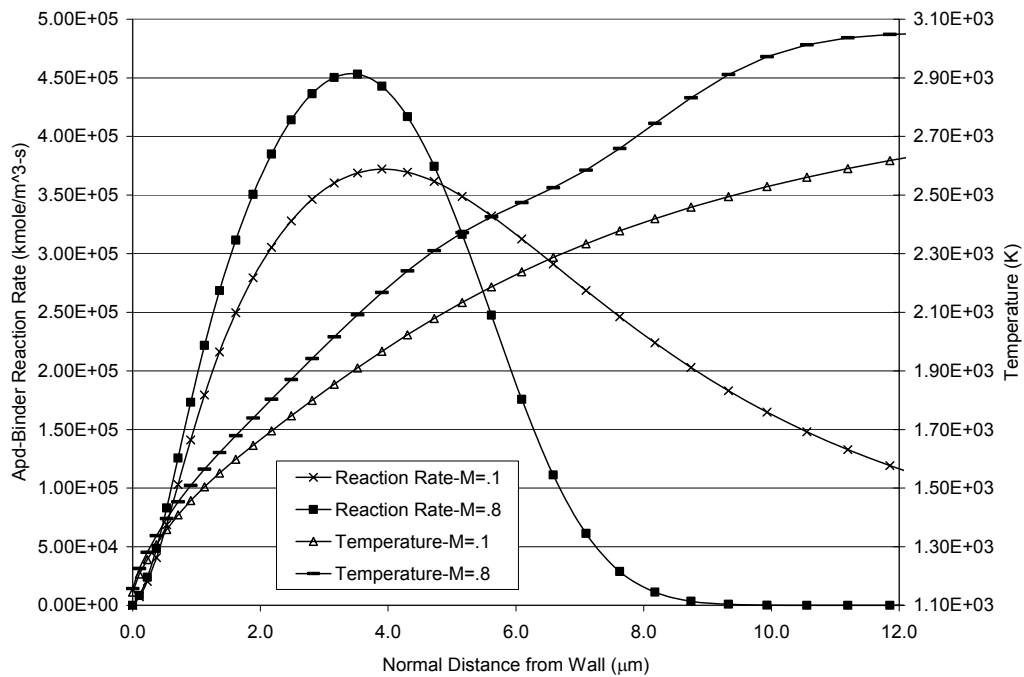


**Figure 38 Comparison of Reaction Rate Gradients to Thermal Gradients**

Figure 38 shows that the thermal gradient is fairly constant from the edge of the thermal boundary down to the wall. No discontinuities are shown in the thermal profile as it passes through the APd-binder flame. Since the regression rate is determined by the energy balance at the solid gas interface, the conclusion is that the controlling parameters in the heat flux to the surface are the surface temperature and the free stream conditions. Although the temperature gradient at the wall varies with Mach Number, it appears to be weakly influenced by the flame zone.

The unsteady velocity fluctuations above the burning propellant and in front of the burning propellant at  $y^+$  locations of 15 and 30 are presented in the appendix. The plots show turbulent intensities of . The result of these fluctuations is evident in the unsteady burning rate and surface temperatures, also shown in the appendix.

### 5.7.5 Reduced Base Burn Rate Analysis

The literature shows that as the base burning rate is lowered, the percent increase in rate due to cross-flow increases. Thus, low burning rate propellants are more affected by cross-flow. This supports the conclusion in the previous section that the flow field dominates the regression rate. If the heat flux into the propellant surface is largely dictated by the cross-flow conditions, then when cross-flow is introduced and the heating rate increases, the surplus energy that is conducted to the surface will be predominantly a function of the free stream Mach Number, and not the base burning rate of the propellant. Consequentially, the propellant's regression rate must rise to meet the heating rate of the free-stream and balance the surplus energy at the surface. Thus, if the required regression is determined by the free-stream, then the percent increase with Mach Number will increase when compared to a lower base rate.

To investigate this, a second analysis is run where the base rate (no cross-flow) is artificially reduced by approximately 50% by increasing the heat of pyrolysis. All other boundary conditions remain the same (i.e. pressure). This model is then subjected to cross-flow for a free stream condition of  $M=0.8$ . Shown in Table 6 are the results of the analysis. The erosive burning rate increases by 53% in the low rate case, as compared to 21% in the high rate case.

**Table 6 Results of the Low Rate Analysis**

	Base Rate (cm/s)	Rate at $M=0.8$ (cm/s)	Ratio ( $r/r_o$ )	Surface Temperature (K) at $M=0.8$
Low Rate	2.698	4.128	1.53	1111.72
High Rate	5.295	6.453	1.21	1167.22

The following plots show a comparison of these results to the M=0.8 results in the previous analysis.

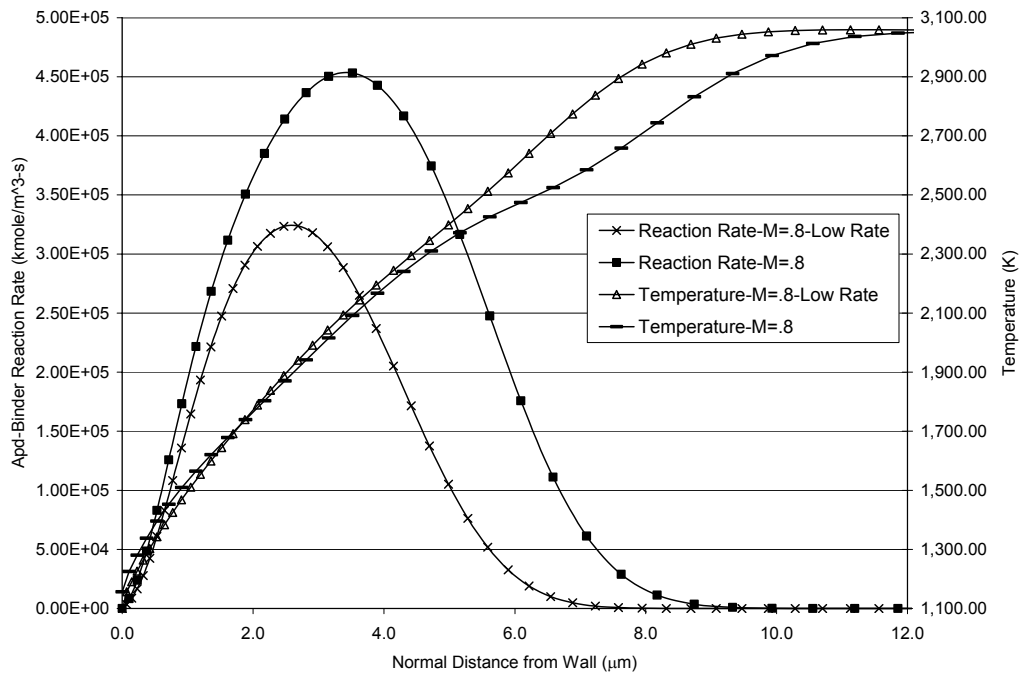


**Figure 39 Comparison of Thermal Gradients Through the APd-Binder Flame for a High Rate and Low Rate Propellant**

Figure 39 shows a comparison of the thermal gradients for the high and low rate propellants through the premixed APd-binder flame. The high rate curve shows the edge of the thermal boundary layer to be further from the wall, representing more heat loss to the wall. However, both curves converge at a distance from the wall beyond either flame, and continue to the wall at approximately the same slope. Figure 40 shows that the point of maximum vorticity moves closer to the wall with the lower burn rate. This is to be expected since the lower injection velocity in the low rate case will not displace the velocity boundary layer as much. Of note is that the APd-binder flame thickness is

reduced in the low rate case in proportion to the movement of the maximum vorticity location.

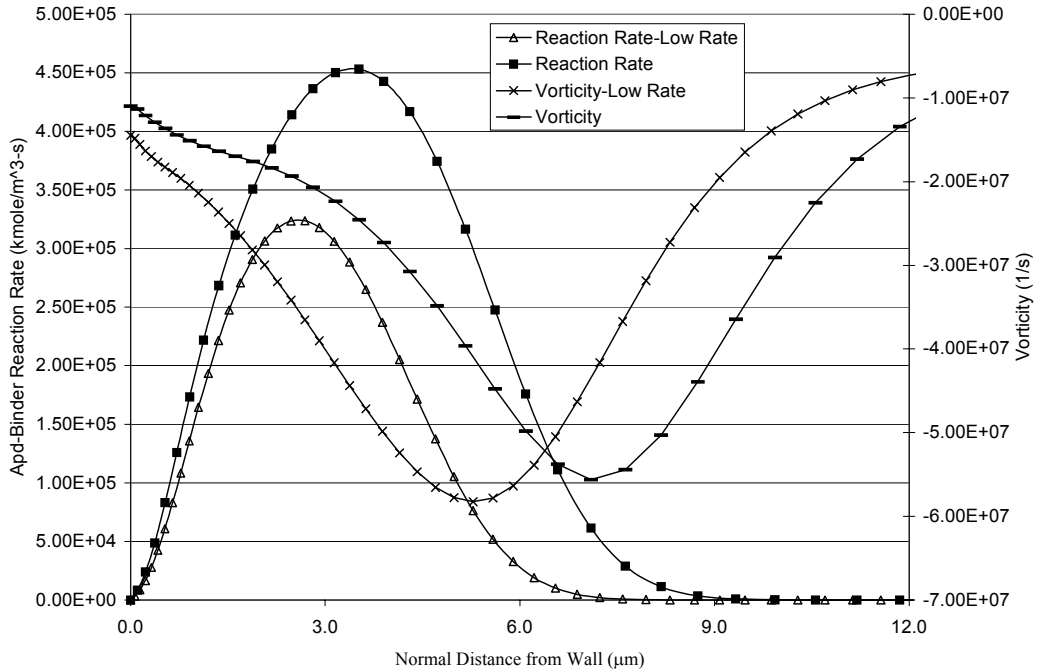


**Figure 40 Comparison of Vorticity Through the APd-Binder Flame for a High Rate and Low Rate Propellant**

Figure 41 shows a comparison of the thermal gradients at the solid-gas interface between the two cases. On the gas side, the heating rate converges in slope from approximately 5 microns down to the wall. The solid side shows a distinct difference in slope. The low rate propellant allows the surface heat to penetrate further into the solid resulting in a shallower slope at the surface, and less heat loss from the free-stream. The high regression rate keeps the thermal gradient high on the solid side, which results in more heat loss from the free-stream.

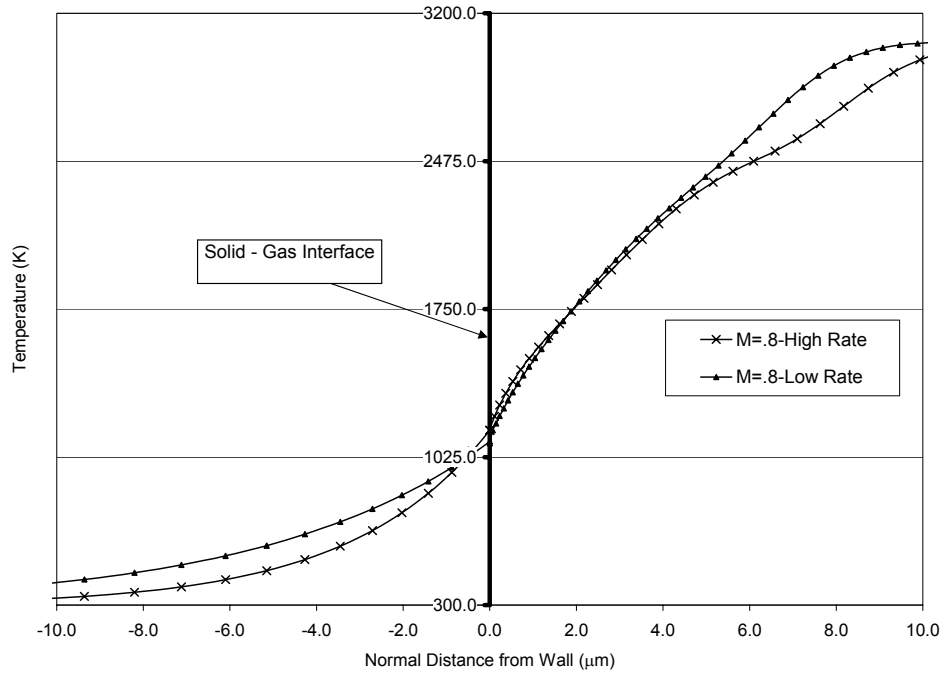


**Figure 41 Comparison of Thermal Gradients at the Solid-Gas Interface for a High Rate and Low Rate Propellant**

Figures 42 through 45 show various flow contours at  $M=0.0$ , and  $M=0.3$  free-stream conditions. The contours illustrate the bending of the normal stream lines near the burning propellant as the Mach Number increases.

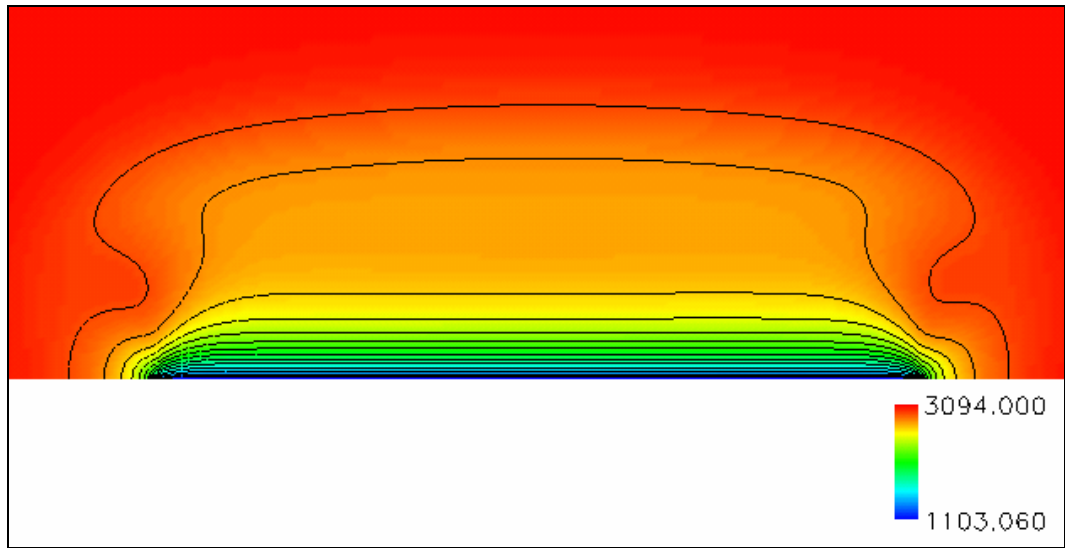


Figure 42 Temperature Contours for  $M=0.0$  (K)

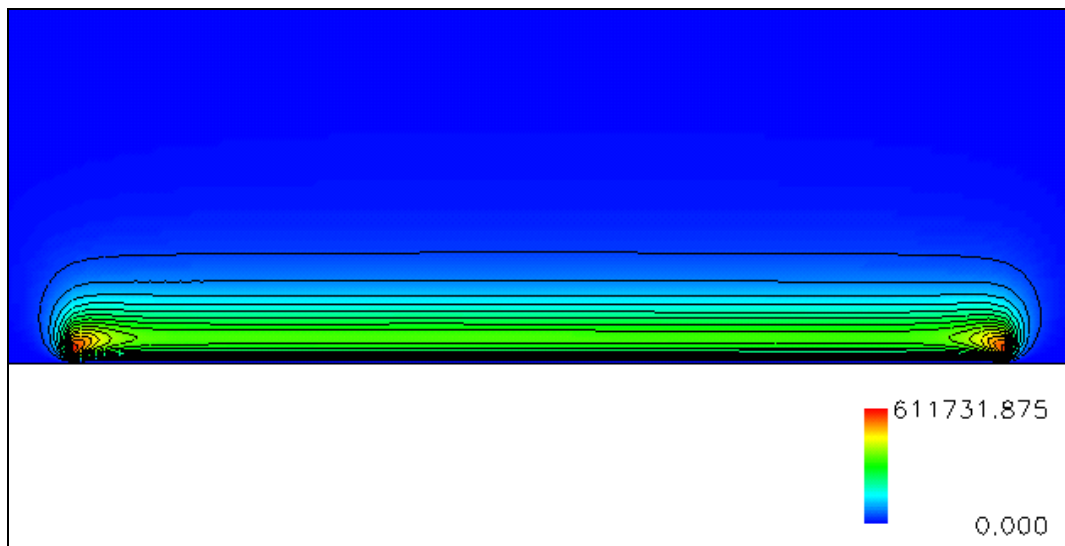


Figure 43 APd-Binder Reaction Rate Contours for  $M=0.0$  (K)

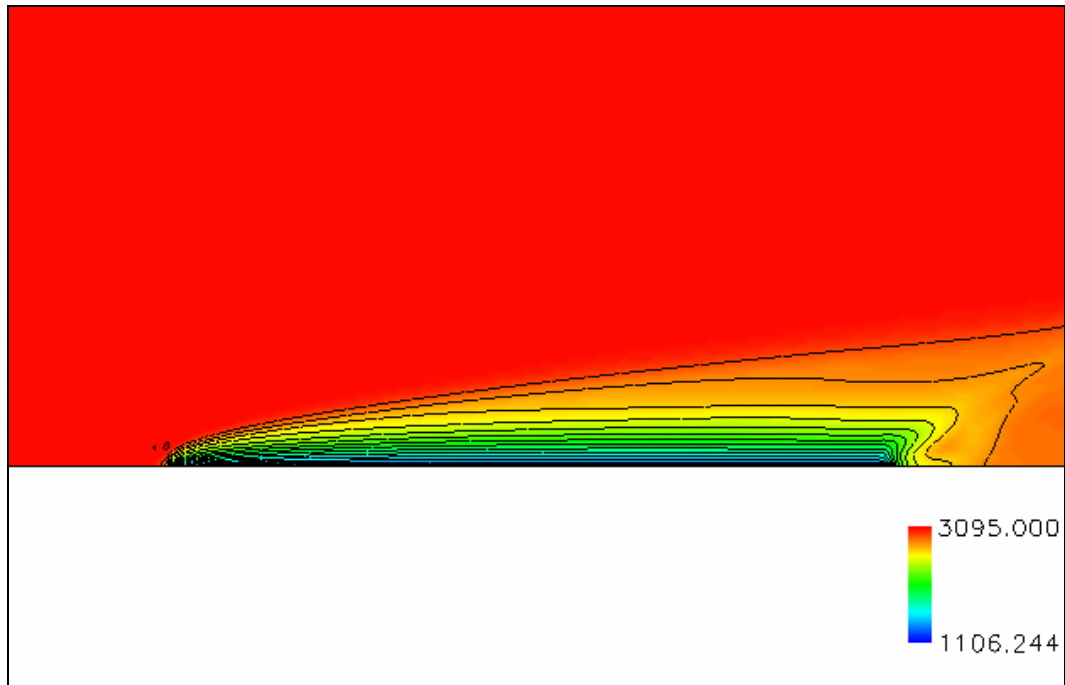


Figure 44 Temperature Contours for  $M=0.3$  (K)

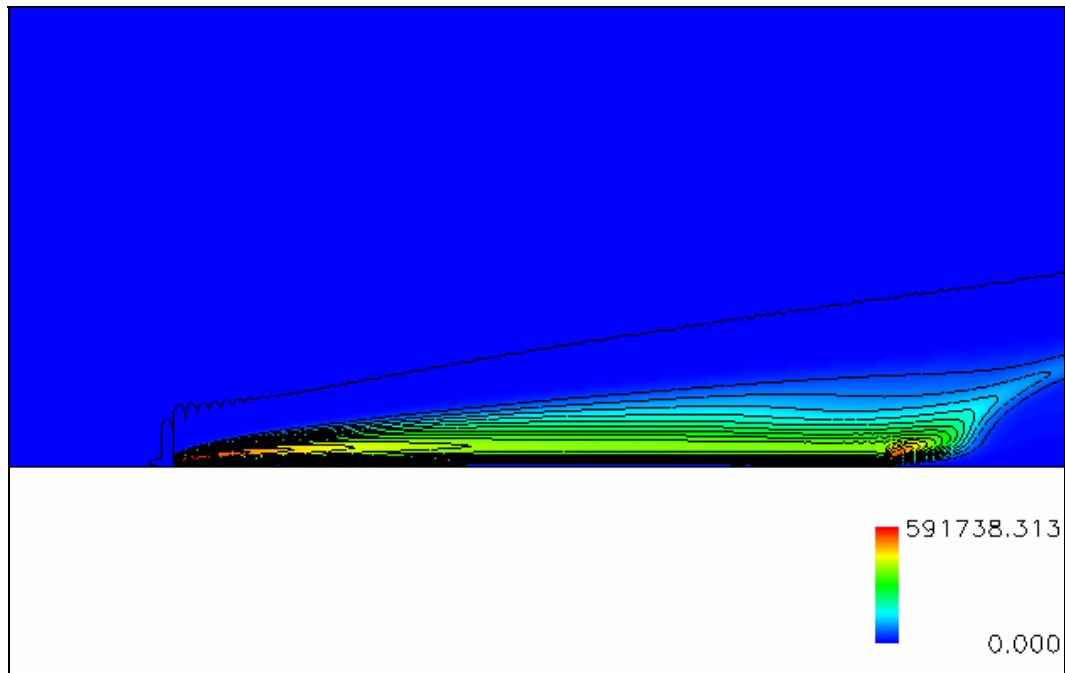
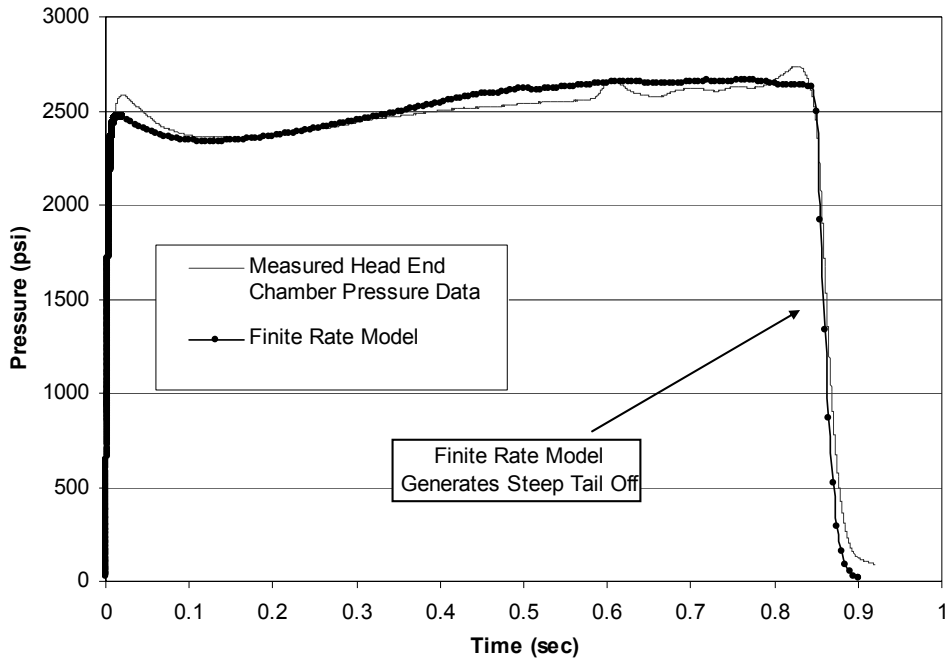


Figure 45 APd-Binder Reaction Rate Contours for  $M=0.3$  (K)

### *5.7.6 Interior Ballistics Results for Finite Rate Model*

Figure 46 shows the results of the interior ballistics analysis compared to the CKEM-4 static test data using the finite rate model. The model shows a reasonable match on the start-up transient. During this part of the motor operation, the internal Mach Numbers will be the highest. However, the plot shows that the predicted tail-off of the finite rate model is too steep in slope. The shallower tail-off that is seen in the test data occurs when longitudinal propellant slivers are created in a motor due to burn rate gradients in the axial direction. This occurs in a simulation when the erosive burning model correctly predicts the erosive burning level versus Mach Number. The steep tail-off and the under prediction of the start-up transient indicate that the erosive burning model is under predicting the erosive rate versus Mach Number. The match between the test data and the simulation is very good in light of the fact that the DNS model was applied to strand burn rate data directly and then used to predict the motor pressure. Refer to Figure 3 to see the prediction of the motor pressure using strand data alone. Although many assumptions were made in the analysis, one source of error is that the DNS model was generated for one base rate taken at the average motor pressure. As is shown in the previous section, the relationship between the erosive amplification factor and base burn rate is not constant. In addition, in the finite rate model three temperature rate equations are introduced, where the temperature dependency of each must be assumed. As the analysis shows, the surface temperature rises very little, so the heat transfer to the surface from the fluid is dictated by changes in the flow field. The Arrhenius type pyrolysis law is used to relate the propellant's pyrolysis rate to the surface temperature. The

temperature dependency of this equation is not calibrated in the DNS analysis, but is taken from the literature.



**Figure 46 Interior Ballistics Results with Finite Rate Model**

The local burning rates as a function of axial distance from the head end of the motor, as calculated in the interior ballistics analysis, are shown in Figure 47 for a slice in time shortly after ignition. Also shown in the figure is the base rate calculated at the local static pressure conditions (no erosive burning). The decrease in the base rate in the axial direction reflects the decrease in the static pressure as the Mach Number increases toward the aft end. The plot shows that the largest percent increase occurs at the aft end, as expected, since the aft has the highest Mach Number. However, the highest overall rate occurs at approximately  $2/3$  from the head end, where the combination of local pressure

and local Mach Number combine for the largest total rate. The plot serves to illustrate the variation in base rate along the motor axis at a given slice in time, and explains slivers.

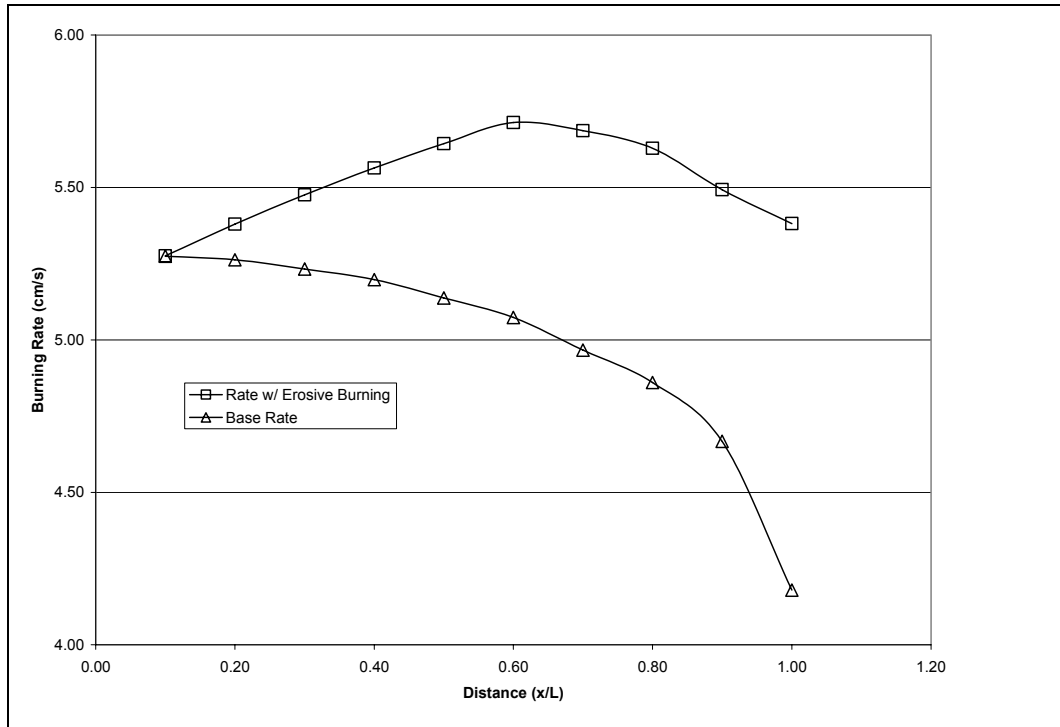


**Figure 47 Erosive Burning Rate Compared to the Base Rate**

## CHAPTER 6

### CONCLUSIONS AND FUTURE WORK

The primary objective of this work is to demonstrate that an erosive burning model can be developed through DNS that is based on, and calibrated to strand burn rate data. Two approaches are used, a finite rate model, and an infinite rate model, to isolate different erosive burning mechanisms and demonstrate the relative importance of each on the erosive burning phenomenon. The results of the models generated with DNS have been incorporated into an interior ballistics analysis for the purpose of predicting the chamber pressure of an actual full scale motor, and compare the predictions to test data. The results of both models show very good agreement to the test data, with the infinite rate model showing the best match at lower Mach Numbers. The models are also shown to be loosely dependent on the full scale motor geometry, and primarily dependent on the combustion gas, and solid propellant physical properties. The results are considered valid for small, evenly distributed AP, where the assumption of premixed APd-Binder gases is reasonable.

The results of this study are significant in that a method for bridging the gap between subscale test data and full scale design and analysis has been demonstrated. Unlike current erosive burning models that depend heavily on the full scale geometry or flow features, the DNS approach is calibrated to strand burn rate data, and a specific propellant's solid and combustion gas thermophysical properties. This feature is significant in that the model can be used predictively during an initial design phase

where the geometry may experience several modifications, but the propellant choice remains constant.

The difference between the predictions of the infinite rate model and the finite rate model can be attributed to the ability to calibrate each to the strand burner test data. The infinite rate model is a heat transfer based model entirely. When using temperature independent thermodynamic properties of the gas, the heat transfer model is fully calibrated to the strand burn rate data through one variable, either the assumed surface temperature, or the heat of pyrolysis. The resulting regression rate is based solely on an energy balance at the gas to solid interface. As the Mach Number increases, boundary layer compression results in an increase in the heat transfer to the surface, which is then balanced by an increase in the regression rate.

For the finite rate model, several additional physical features are modeled. A two-step chemistry model is added, with the addition of a pyrolysis law for the solid. These three additional physical features add three temperature dependent rate equations, which require calibration. However, the  $M=0.0$  calibration analysis is all that is available, and through the adjustment of the surface temperature, the regression rate at the no cross-flow condition is calibrated. This means that the temperature dependency of the rate equations must be assumed.

By use of a two-step finite rate chemistry model calibrated to strand burn rate data, the premixed APd-binder gas flame thickness is shown to reduce due with the cross-flow velocity and is correlated to the near wall vorticity increases that occur with cross-flow. The results also show that the stand off-distance of the APd-binder flame varies little with cross-flow. Plots of the temperature gradients from the thermal boundary layer edge

down to the wall show little variation as the curves pass through the flames, but show considerable dependency on the free-stream condition. A comparison of the temperature slopes near the wall for a high rate propellant and a low rate propellant burning in identical free-stream conditions show similarity, although the mass injection rate, and flame structure are dissimilar. Finally, the comparison of the results of an infinite rate model to the finite rate model show excellent agreement in the erosive amplification factor as a function of Mach Number. In both models, the flow field is equally resolved, with the only difference being the treatment of the heat release mechanism.

The use of a pyrolysis law has also demonstrated that the surface temperature changes very little with large increases in regression rate. This is due to the large activation energy of the pyrolysis process. So, the assumption of a constant surface temperature is very reasonable over a wide range of rates. The advantage of the constant surface temperature approach is that the regression rate is calculated completely from a surface energy balance, which eliminates one temperature dependent equation (pyrolysis law) that can not be calibrated. Many propellant development programs include burn rate testing at several temperature extremes. When available, this data can be incorporated into the calibration process to determine the pyrolysis rate dependency on temperature.

Several areas for improving the model exist, in addition to calibrating the pyrolysis law. The use of an isentropic and adiabatic temperature profile at the domain entrance causes large heat transfer rates at the leading edge of the burning propellant. This also results in an increase in the predicted rate. At low Mach Numbers, this spike diminishes quickly, and a fairly constant rate is seen along the propellant surface. At higher Mach Numbers (greater than  $M=0.3$ ), the spike, coupled with boundary layer

growth, persists over a large portion of the assumed propellant surface length. The addition of a thermally developed profile at the entrance may improve the rate calculations at higher Mach Numbers with the requirement for increasing the domain length. Eliminating the assumption of premixed APd-binder gases will improve the standoff distance calculations. This requires modeling the propellant surface with discrete locations of AP and binder solids.

Both the finite rate model and the infinite rate model produce very good results when incorporated into the interior ballistics code. This supports the conclusion that heat transfer is dominant in the erosive burning problem, since this is the commonality between the two models. The finite rate model has the advantage of correctly distributing the heat release from the combustion process, which gives a more accurate value for the temperature gradient at the wall. The infinite model has the advantage of requiring less assumptions by way of the elimination of the pyrolysis law, and the chemical rate equations, but produces a temperature jump at the wall due to the instantaneous application of the heat release. This is accounted for in the present analysis by calculating the gradient a short distance from the wall, beyond the application of the heat release. A better way may be to assume a mixing length from the wall (20-40 microns based on the finite rate flame thickness predictions), and distribute the heat over this length.

## APPENDIX

### TIME DEPENDENT DATA

Presented in this section are plots showing time dependent data of velocity fluctuations at various locations in the flow-field. The data is taken at points of  $y^+$  values of 15, and 30 for two locations in the transverse direction. One set of points lies in the flow-field above the center of the propellant. The second points lie in a plane that is approximately 4.2% from the entrance.

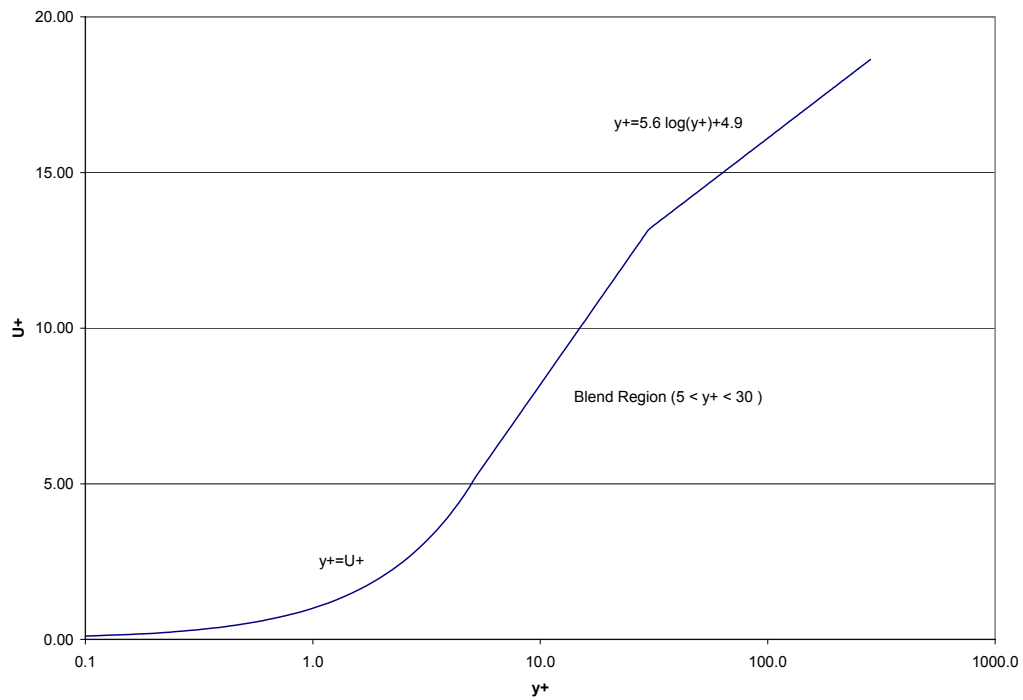
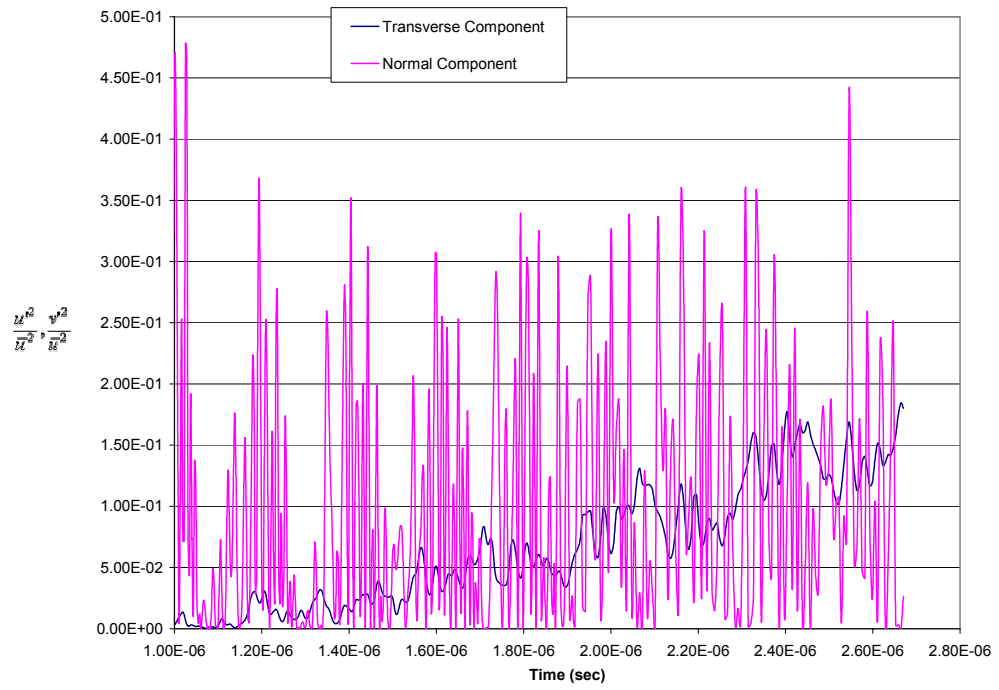
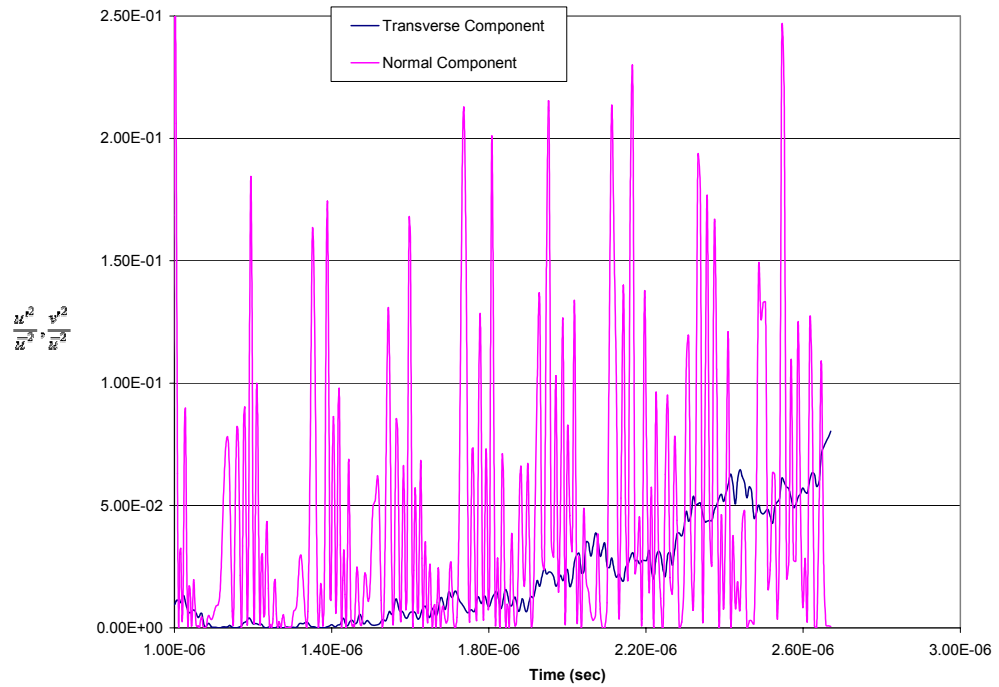


Figure 48 Entrance Velocity Profile in  $Y^+$  Coordinate System



**Figure 49 Velocity Fluctuations at  $y+=15$ ,  $M=0.1$ , Over Center of Propellant**



**Figure 50 Velocity Fluctuations at  $y+=30$ ,  $M=0.1$ , Over Center of Propellant**

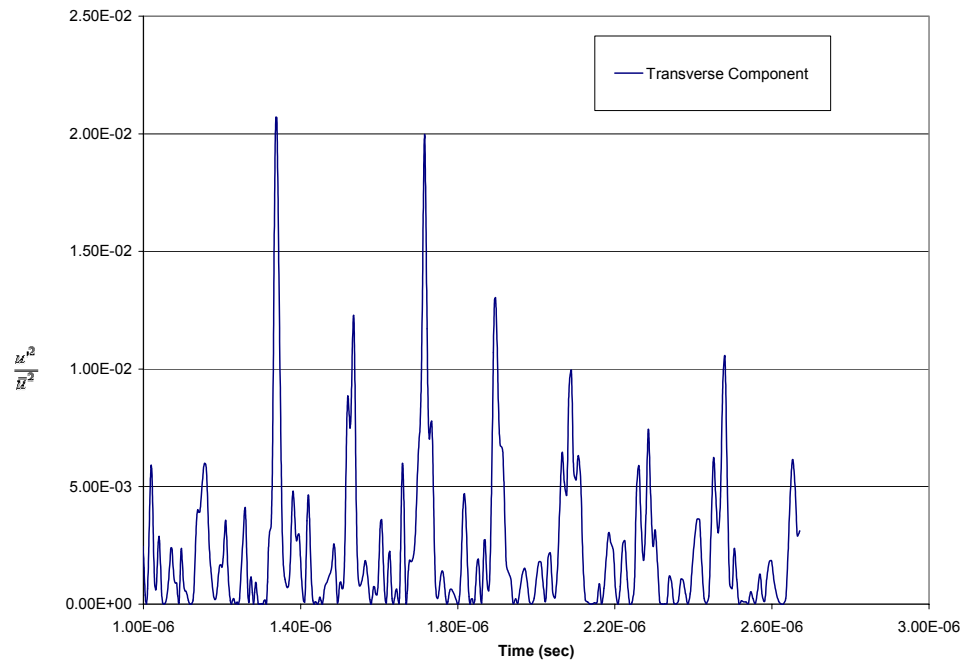


**Figure 51 Velocity Fluctuations at  $y+=15$ ,  $M=0.1$ , Near Entrance**

## REFERENCES

1. Graham, W.H., and Keller, K.D., "Burning Rate Studies with the Micro-Window-Bomb Strand Burner", *Technical Report s-214*, ROHM and HAAS COMPANY Redstone Research Laboratories, February 1969.
2. Sutton, George P., *Rocket Propulsion Elements* (John Wiley and Sons, New York, 1967).
3. Lenior, J.M., and Robillard, G., "A Mathematical Method to Predict the Erosive Burning Effect in Solid Rockets", 6<sup>th</sup> International Symposium on Combustion, Reinhold, NY, 1957.
4. Green, Leon, "Erosive Burning of Some Composite Solid Propellants", *Journal of the American Rocketry Society*, Vol. 24, Num. 1, Jan-Feb, 1954.
5. Kreidler, J.W., "Erosive Burning: New Experimental techniques and Methods of Analysis", AIAA Solid Rocket Conference, Palo Alto, CA, Jan. 1964, Num. 64-155.
6. Williams, Forman A., *Combustion Theory* (The Benjamin/Cummings Publishing Co., Menlo Park, 1985).
7. Razdan, M.K., and Kuo, K.K., "Erosive Burning Study of Composite Solid Propellants by Turbulent Boundary-Layer Approach", *AIAA Journal*, Vol. 17, No. 11, 1979, pp. 1225-1233.
8. Gordon, J.C., Duterque, J., and Lengelle, G., "Erosive Burning in Solid Propellant Motors", *Journal of Propulsion and Power*, Vol. 9, No. 6, 1993, pp. 806-811.

9. Bulgakov, Victor K., and Karpov, Alexander I., "Numerical Studies of Solid Propellant Erosive Burning", *Journal of Propulsion and Power*, Vol. 9, No. 6, 1993, pp. 812-818.
10. King, Merrill K., "Erosive Burning of Solid Propellants", *Journal of Propulsion and Power*, Vol. 9, No. 6, 1993, pp. 785-805.
11. Mukunda, H.S., and Paul, P.J., "Universal Behavior in Erosive Burning of Solid Propellants", *Combustion and Flame*, Vol. 109, 1997, pp. 224-236.
12. Apte, Sourabh, and Yang, Victor., "Turbulent Flame Dynamics of Homogenous Solid Propellant in a Rocket Motor", *Proceedings of the Combustion Institute*, Vol. 28, 2000, pp 903-910.
13. Kennedy, C.A., and Carpenter, M.H., "Comparison of Several Numerical Methods for Simulation of Compressible Shear Layers", *NASA Technical Paper 3438*, Langley Research Center, December 1997.
14. Jackson, H. A., Buckmaster, T.L., and Stewart, D.S., "Nonsteady Burning of Periodic Sandwich Propellants with Complete Coupling between the Solid and the Gas Phase", *Combustion and Flame*, Vol. 125, 2001, pp. 1055-1070.
15. Gordon, S., and McBride, B.J., "Computer Program for Calculation of Complex Chemical Equilibrium Compositions, Rocket Performance, Incident and Reflected Shocks, and Chapman-Jouguet Detonations", NASA SP 273, 1971.
16. Poinot, T.J., and Lele, S.K., "Boundary Conditions for Direct Simulations of Compressible Viscous Flows", *Journal of Computational Physics*, Vol. 101, 1992, pp. 104-129.

17. Cazan, R. and Menon, S., "Direct Numerical Simulation of Sandwich and Random-Packed Propellant Combustion", 39<sup>th</sup> *AIAA/ASME/SAE/ASEE Joint Propulsion Conference*, AIAA 2003-5082, July 2003.
18. MacCormack, R.W., "The Effect of Viscosity in Hypervelocity Impact Cratering". AIAA, 1969, paper number 69-354.
19. Chattot, Jean-Jacques. *Computational Aerodynamics and Fluid Dynamics, An Introduction*. Springer, New York, 2002, pp. 44.
20. McDonald, Brian A., and Maykut, Albert, R., "A New Finite Element Based 1-D, Unsteady Finite Differencing Ballistics Code", JANNAF Propulsion Conference, Tampa, FL. December 4-8, 1995.
21. Lax, P., and Wendroff, B., "Systems of Conservation Laws", *Comm. Pure Applied Math.* 1960, Vol. 13, pp. 217-237.

## **VITA**

Brian McDonald is the Vice President and Technical Director at Stone Engineering Company in Huntsville, AL. Stone Engineering is a propulsion research and development company that supports Strategic and Tactical Missile System programs of both the U.S. Army and Navy. Mr. McDonald lives in Taft, TN with his wife, Piper, and three daughters, Kaleigh, Kelsey, and Sarah.